Fatigue Crack Growth behavior of Additively Manufactured 17-4 PH Stainless Steel: Effects of thickness and surface condition

NTNU

Norwegian University of Science and Technology

Institutt for maskinteknikk og produksjon

Master Course in Mechanical Engineering

Academic year 2022/2023

Advisor: Prof. Seyed Mohammed Javad Razavi   Author: Davide Agiollo

Co-advisor: Pietro Foti

Contents

List of Figures

List of Tables

Abstract

Additive Manufacturing (AM) revolutionized the field of manufacturing by enabling the production of complex geometries with greater design freedom. However, the use of these components for structural applications depends on a proper understanding of their mechanical behavior, which may differ significantly from that of traditionally manufactured counterparts. This study aims to investigate the Fatigue Crack Growth (FCG) behavior of 17-4 Precipitation Hardening (PH) Stainless Steel (SS) obtained via Laser Powder Bed Fusion (L-PBF). Four sets of Compact Tensile (CT) specimens were tested to investigate the fatigue crack growth properties of the material analyzed. Different procedures can be considered for this kind of tests; in the present study the constant amplitude procedure was considered. The objective of the tests was to characterize the Paris regime and assess the influence of thickness and surface condition on the Fatigue Crack Growth properties. In order to gain insights into the mechanisms of crack growth, macro-graphic observations and Scanning Electron Microscope analysis were carried out to study the microstructure and the fracture surface. The results of these analyses revealed no significant differences in the behavior among the specimens of different sets. This finding was attributed to the low presence of defects and the isotropy of the material, resulting from the CA-H1025 heat treatment to which the specimens were subjected.

Notation

AM	Additive manufacturing	NS	Net shape
PH	Precipitation hardening	SM	Shallow machined
SS	Stainless steel	DM	Deep machined
SLM	Selective laser melting	SR	Stress relief
LB-PBF	Laser-beam powder bed fusion	YS	Yield strength
AB	As built	UTS	Ultimate tensile strength
HT	Heat treated	EF	Elongation to fracture
ST	Solution treated	FCG	Fatigue Crack Growth
AG	Age hardening treatment	da/dN	Fatigue crack growth rate
AC	Air cooling	ΔK	Stress intensity factor range
EDM	Electro Discharge Machining	ΔK_{th}	Threshold stress intensity factor range
M	Martensite	C, m	Paris equation coefficients
A	Austenite	R	Stress ratio

1 Introduction

In the last decades numerous studies have been conducted on mechanical characterization of metals produced with Additive Manufacturing (AM) techniques. The main aim of these studies is to correlate the mechanical properties with the typical features present in components made with this technology. In fact, AM components have a different microstructure and a defects distribution compared to the conventional counterparts. In this scenario, understanding the correlation between process parameters, microstructure and mechanical performance is fundamental to optimize the process and develop new materials. Moreover, a better characterization of static and fatigue behavior guarantees the application of safe life approaches in the design of components, and lastly, the knowledge of the fracture behavior permits the application of damage tolerant approaches that fit well with the typical applications of AM products.

17-4 Precipitation Hardened Stainless Steel is a high strength martensitic steel, suitable for production through additive manufacturing technologies due to its specific mechanical properties, that permits applications in aerospace, automotive and chemical industries. The high strength derives from the presence of the hard martensitic phase [1] and from the precipitation hardening, occurring while aging at 482°C [2] after the solution heat treatment [3].

In 2010, Facchini et al. [4] studied the static mechanical properties of 17-4 PH SS produced by selective laser melting, with a particular focus on the effects of metastable austenite. The specimens for the tensile tests were vertically built under Argon atmosphere, and after building, heat treated at 600°C for 2 hours. In the study, it is reported how the large solidification undercooling may prevent the formation of martensite in the as-built material. The result is a prevailing austenitic microstructure with high work hardening behavior, characterized by more than 1 GPa of tensile strength and more than 20% of elongation at fracture. The same results were found by Murr et al. [5] in 2012, with the introduction of one of the most debated topics of AM 17-4 PH stainless steel production, the building gas.

In 2014, Stucker et al. [6] studied the evolution of the microstructure and its effect on the static mechanical properties of 17-4 PH SS processed by SLM. The samples for

the tests were built with the same process parameters, except for the process environment: half of the samples were produced under an Argon atmosphere and the other half under Nitrogen atmosphere. During the post-processing, the samples were machined and subjected to three different heat-treatments: 650°C for 2 hours, 788°C for 2 hours and 788°C for 2 hours + 482°C for 1 hour. The results were finally compared to the as-built parts: in both cases the as-built parts have lower yield and ultimate tensile strength compared to heat treated samples (results reported in Table 1). The building environment has a strong effect on the final microstructure, as parts built under Nitrogen atmosphere contained a mixture of martensite and retained austenite, while parts built under Argon atmosphere had a predominantly martensitic structure, with a small amount of retained austenite. It is important to underline how the presence of retained austenite is detrimental or beneficial depending on the application, in fact, it allows more plastic strain prior to crack initiation, but although it is good for toughness, it has detrimental effects on the tensile properties.

The previous results were also confirmed by the review of Ramamurty et al. [7], that systematically compared different studies regarding the static mechanical behavior of 17-4 PH SS, reporting similar conclusions. The static mechanical properties, as gathered by Ramamurty et al. [7] are reported in

Table 1.

Even though the static behavior of AM 17-4 PH SS is comparable –and sometimes even better– than the same material obtained with the traditional subtractive technology, additively manufactured components are usually characterized by the presence of several defects having various morphologies that severely affects the fatigue behavior of such components. Their fatigue behavior is, as a matter of fact, more complex and challenging; besides, the dynamic response of these components cannot be neglected being the fatigue failure the most common reason of mechanical failures of engineering parts and structures. In addition, in the last few years also the fracture behavior has been investigated, with a particular focus on the effects of process parameters and post process treatments.

Table 1

Tensile properties of 17-4 PH SS produced by different processes and heat treatment conditions.

Alloy	Process	Source	Condition	Microstructure	YS [MPa]	UTS [MPa]	EF [%]
17-4 PH	Wrought	[8]	ST+AG	M	1170	1310	10
		[9]	-	-	1235	1279	33.6
	LB-PBF		ST (1050°C for 0.5 h, AC) + AG (552°C for 4 h, AC)	-	1154	1193	21.2
		[5]	AB	M	1190	1370	8.3
		[10]	AB	64% M, 36% A	661±24	1260±3	16.2±2.5
			AG (480°C for 1 h, AC)	59.5% M, 40.5% A	945±12	1420±6	15.5±1.3
			AG (620°C for 4 h, AC)	94.4% M, 5.6% A	1010±15	1320±2	11.1±0.4
			ST (1040°C for 0.5 h, AC)	M	939±9	1190±6	9±1.5
			ST (1040°C for 0.5 h, AC) + AG (480°C for 1 h, AC)	96.7% M, 3.3% A	1350±18	1440±2	4.6±0.4
		[4]	AG (600°C for 2 h)	28% M, 72% A	600	1300	28

In 2020, Nezhadfar et al. [8] studied the effect of building gas, investigating the reason for how it is an in-process refinement of microstructure and defects technique, and consequently how it affects the mechanical properties. Axial fatigue specimens and compact tensile specimens were tested respectively for fatigue and fracture characterization, all vertically built and subjected to CA-H1025 heat treatment (solution heat treating at 1050°C for 0,5 h followed by air cooling and then aging at 552°C for 4 hours followed by air cooling, utilizing an argon atmosphere box). The effects in the fatigue life for use of N_2 as shield gas must be attributed to a finer microstructure containing more retained austenite and to pores size and quantity, that are smaller and fewer than in argon shield specimens. This is due to the possibility for nitrogen to be absorbed in the meltpool. Consequently, fatigue life for specimens built

3

under N_2 considerably increases in high cycle life (for a stress amplitude of 500 MPa, the reversals to failure can be 10 times greater, from 10^6 for Ar, to 10^7 for N_2). Regarding the fatigue crack growth tests, for the same reasons related to a micro-/defect-structure, in the near threshold zone, Argon specimens have less FCG resistance, while in the Paris regime the behavior is approximately the same. In regime III, specimens built under N_2 atmosphere exhibit higher fracture toughness, and this has to be attributed to the lower amount of defects. The quantitative results are reported in Figure 1, and the Paris Law parameters in Table 2.

Table 2

Paris Equation coefficients obtained from experimental data fitting, Nezhadfar et al. [8].

	$C \left[\frac{m}{cycle} \frac{1}{(MPa\sqrt{m})^n} \right]$	n
HT-N_2	$3{,}6 \times 10^{-8}$	2,7
HT-Ar	$3{,}9 \times 10^{-7}$	2,1
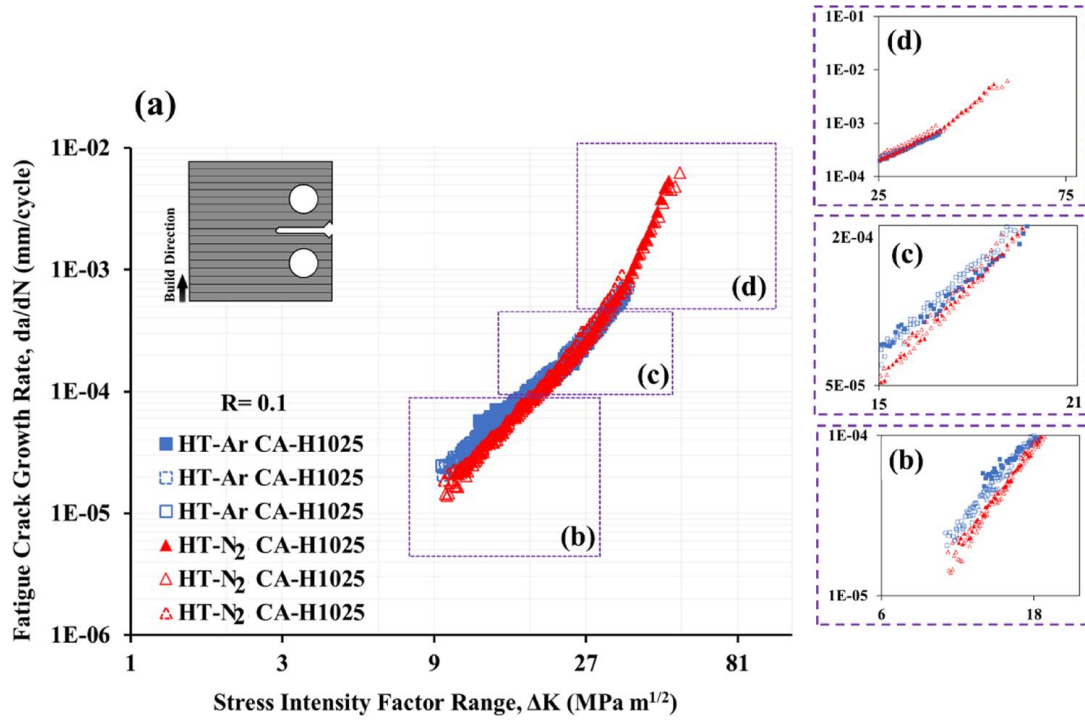
Figure 1: *Fatigue crack growth rates of AM 17-4 PH SS built under N$_2$ and Ar atmosphere, heat treated with CA-H1025 (a), in the 3 different regions: near-threshold (b), Paris Regime (c) and unstable (d). Figure taken from* [8].

The effect of the building orientation was investigated in 2016 by Mower and Long [9]. They conducted a study over the effect of this parameter on the fatigue life behavior of 17-4 PH SS, and then an interesting comparison between AM and traditional techniques specimens. The tensile specimens were built horizontally and vertically, and then heat treated at 788°C for 1 hour. The tests were conducted in rotating bending. The obtained results show a similar trend to the one observed for the static tests; however, in this case, it has never been reported an improvement of properties if compared to the wrought machined counterparts. According to Mower and Long [9], horizontally built material has a fatigue behavior comparable (90%) to that of the conventional material (≈900MPa), while the vertically built showed non comparable results. In fact, fatigue strengths from 25% to 75% of that of horizontally built specimens were found.

In 2019, Shamsaei et al. [10]conducted a study on the effect of the same parameter on the fracture behavior of 17-4 PH SS, considering also the influence of heat treatment post-processing. Compact tensile specimens (Figure 2), under Argon environment, were fabricated both vertically and horizontally and were subjected to two different

5

heat treatments: CA-H900 and H1025. Finally, the results were compared to those of the wrought counterparts.
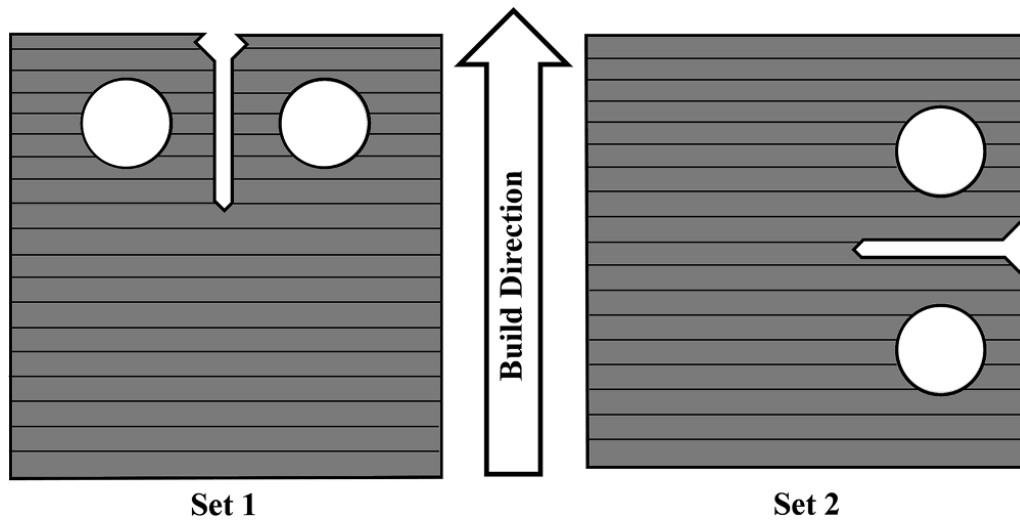
Figure 2: *Drawings of CT specimens used for the FCG tests, with notch parallel (set 1) and perpendicular (set 2) to the building direction. Figure taken from* [10].

The microstructure obtained with the heat treatments was completely martensitic, but some relevant differences were noted: after the H1025 the columnar grains are elongated parallel to the building direction, while after the CA-H900, all the microstructural features such as elongated grains and meltpools disappear. In other words, the CA-H900 is capable of homogenizing the microstructure and H1025 leads to a sparsely distributed precipitates, resulting in a higher ductility. These properties determined also important consequences in the tests: all the specimens of set 1, subjected to H1025, were not tested due to a crack formation during the heat treatment. This phenomenon has been ascribed in the literature to the segregation of Cu an Ni that forms austenite with low strength and to the presence of brittle ferrite in the martensite matrix. For specimens of set 2 the crack started as mode I, but deviates during the test becoming a mode II crack violating the test requirements of ASTM E647[11]. This was also observed by Rack and Kalish [12], that attributed this behavior to the weak interface between ferrite and martensite grain boundaries. Another interesting phenomenon occurs: while the primary crack changes to mode II propagation, a secondary crack were observed, as can be seen in Figure 3.
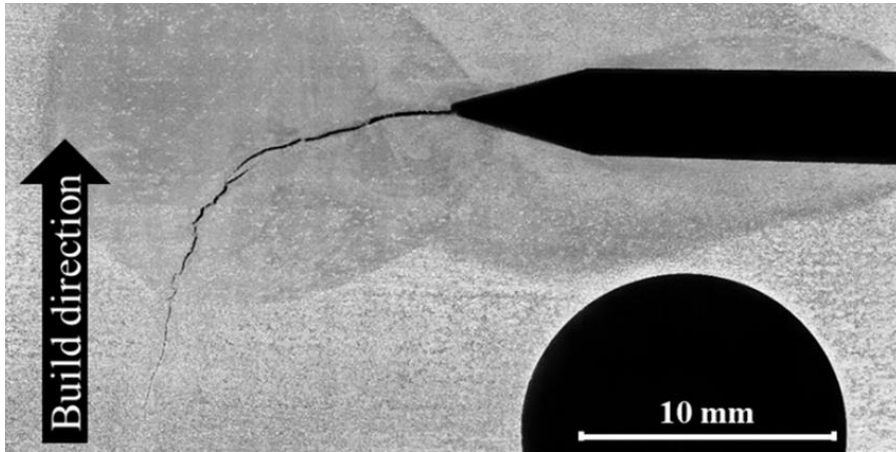
Figure 3: *Macro image of a secondary crack occurring in 17-4 PH SS CT specimens heat treated with H1025. Figure taken from* [10].

Due to these features described in the above, the only valid FCG tests were conducted on the CA-H900 heat treated specimens. The reason has to be ascribed to the primary solution heat treatment step (CA), in which fine austenite grains, in the cooling step, transform to fine martensite, resulting in a higher material strength. The results are reported in Figure 4:
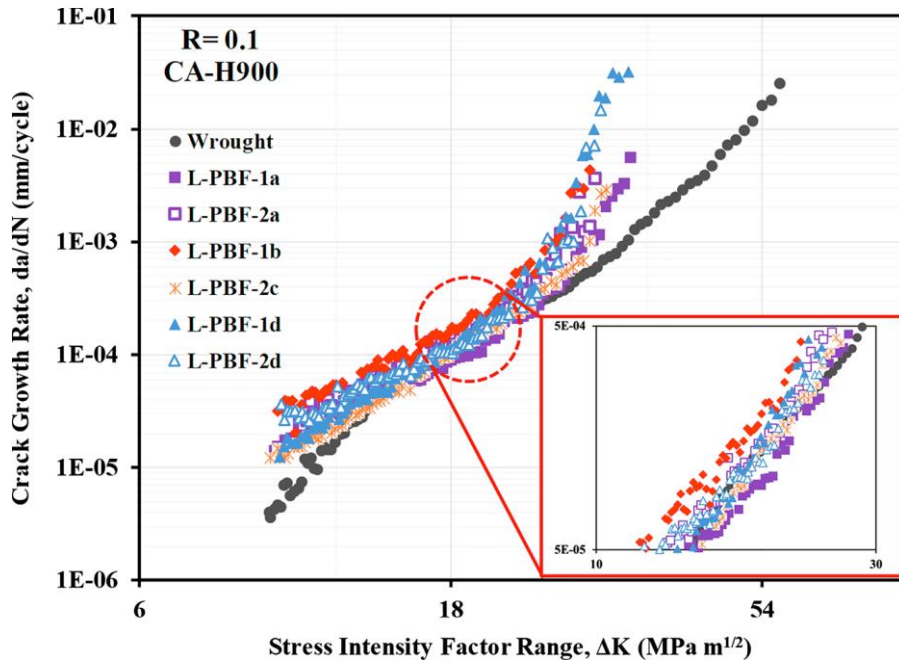
Figure 4: *Fatigue crack growth rate experimental data of LB-PBF and wrought 17-4 PH SS subjected to CA-H900 heat treatment. Figure taken from* [10].

The three typical regions can be identified; moreover, a comparison with the wrought counterparts was made. In the near-threshold region, the wrought material exhibits

7

higher crack growth resistance if compared to the LB-PBF one. The Paris Region is characterized by similar behaviors, and it is important to underline that there is insignificant difference between set 1 and set 2. This is due to the CA-H900 heat treatment, that permits to obtain a homogenous fine microstructure and to remove any residual stresses induced from the process. Finally, in region III, the wrought material shows a higher cyclic fracture toughness. An analysis of the experimental results suggests that region I and region III are critical for the LB-PBF material due to the higher sensitivity of the material to microstructural features in those regions.

In 2017, Yadollahi et al. [13] focused their study on the effect of the heat treatments on the tensile and fatigue behavior of 17-4 PH SS, by comparing heat treated and non-heat treated tensile specimens, built under argon atmosphere, half horizontally and half vertically. The heat treatment examined was the CA-H900, consisting in 30 minutes at approximately 1040°C, air cooling and then precipitation hardening for 1 hour at 482°C. Regarding the static properties, monotonic tension tests were conducted, and the results are reported in Figure 5.
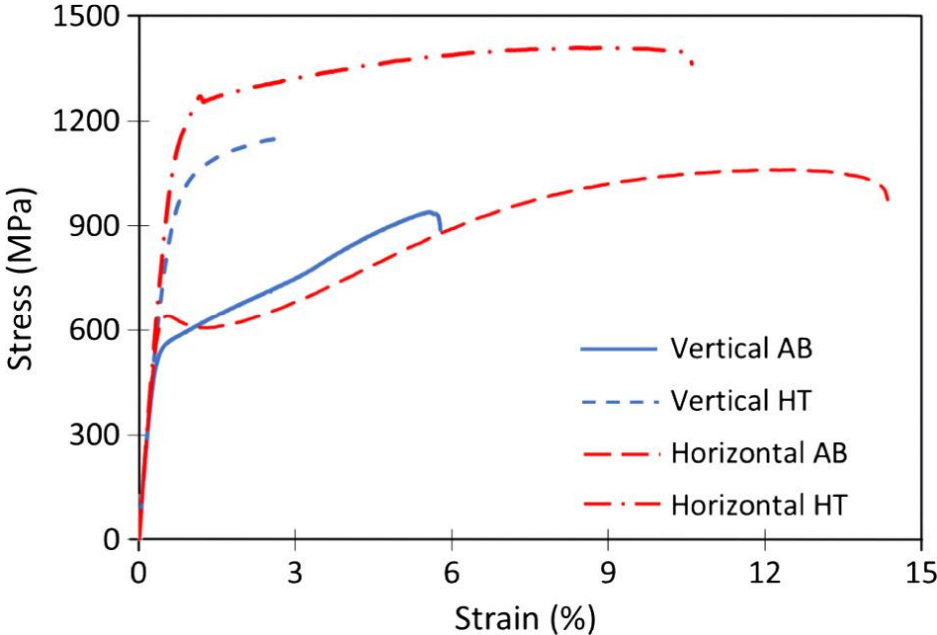
Figure 5: *Engineering stress versus strain curves of LB-PBF PH 17-4 SS, horizontally and vertically built and subjected to CA-H900 heat treatment. Figure taken from [13].*

The modulus of elasticity measured is 187 GPa, while the yield strength for the vertical built specimens is 580 MPa for the as built and 1020 MPa for the heat treated, while, for the horizontally built, it is 650 MPa for the as built and 1250 MPa for the heat treated, with an improvement of the static properties of about 75% and 90% respectively. In both cases the static properties are significantly lower if compared to the wrought material, but for the horizontally-built heat treated one the value is comparable. Regarding the fatigue properties, the results are reported in Figure 6, with the plot of the reversals to failure versus stress amplitude:
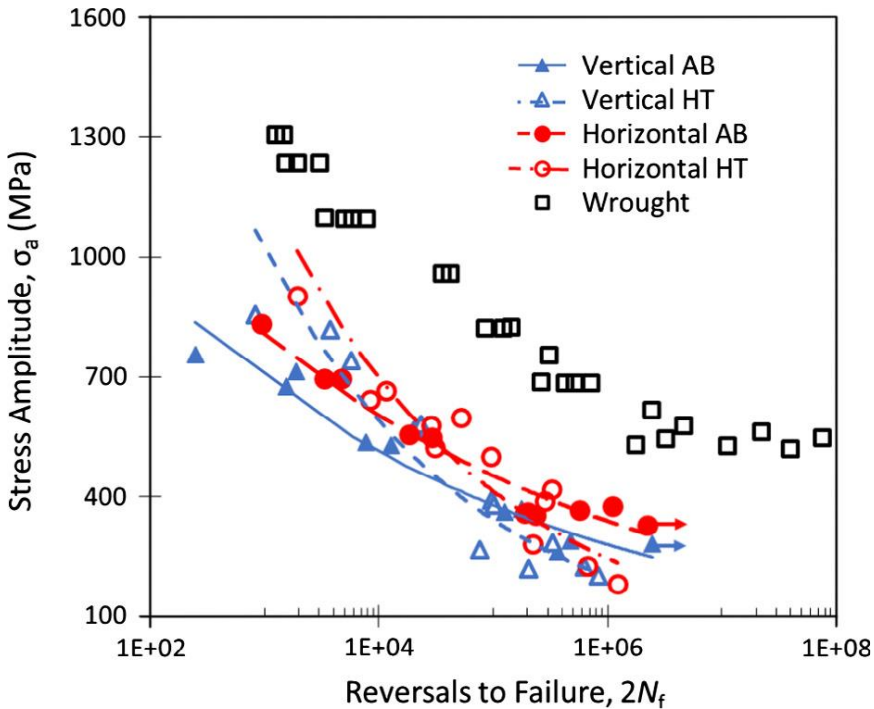
Figure 6: Fatigue stress life data of LB-PBF 17-4 PH SS horizontally and vertically built subjected to CA-H900 heat treatment, compared to wrought 17-4 PH SS subjected to H1050 heat treatment. Figure taken from [13].

In this case the comparison with the 'wrought' material comes from literature data[14], and it corresponds to values of polished flat specimens, heat treated according to H1050 condition. Despite of this, it is shown a significantly shorter fatigue life for AM specimens, and this can be attributed to the higher size and amount of defects.

Three years later, in 2020, Yadollahi et al.[15] investigated the effect of heat treatment focusing on the FCG behavior. The sample were produced with 17-4 PH SS powder, under Argon atmosphere, and they were 'modified compact specimen' (compact specimen with the pins located further from the notch). The notches were obtained

perpendicular and parallel to the building direction, to evaluate the anisotropy of the material. The heat treatment studied was solution annealing for 30 minutes at 1040 °C, air cooling, age hardening for 1 hour at 482°C. To summarize, three sets were studied: as built with transverse crack, as built with longitudinal crack and heat treated with transverse crack, where transverse means perpendicular to the build direction and longitudinal means parallel to the build direction. All the specimens were pre-cracked under constant amplitude compression-compression loading (R=22 or 40 defining the load ratio as between the minimum and the maximum value in compression) for about 38000 cycles. Then, three different test strategies were used: constant K_{max} testing, where the K_{max} is constant while the K_{min} is slowly increased, so that ΔK decrease and it is possible to investigate the threshold region, constant amplitude loading, that made after this kind of pre-cracking, should permit to study the threshold region (because of the lower residual stresses), and the load reduction test (ASTM E-647). A scheme of the test strategies is reported in Figure 7. The microstructure obtained in the samples was characterized by a large presence of un-melted regions and high amount of retained austenite in the plane perpendicular to the building direction; these can be ascribed, respectively, to the laser process parameters, and to the presence of columnar grains, resulting from the heat flux generated during the process.
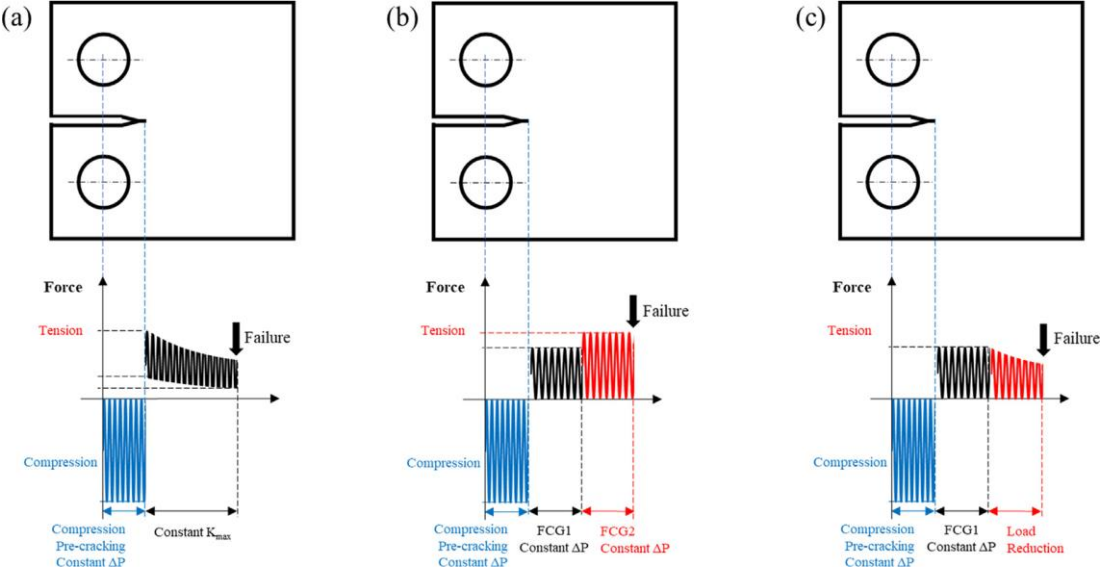
Figure 7: *Load history of the different fatigue crack growth tests: a) compression pre-cracking and constant K_{max} testing, b) compression pre-cracking and constant*

amplitude loading (R=0), and c) compression pre-cracking and load reduction
loading (R=0). Figure taken from [16].

The results show more scatter if compared to wrought alloys, and this can be attributed to the presence of lack of fusion defects and residual stresses. It is important to underline, however, that among the main purposes of the work there was to validate new methods to produce data for the threshold region because of the difficulty in investigating it. The different testing strategies resulted in obtained data, is a threshold of about 5.5 MPa√m, and an estimated fracture toughness of 70 MPa√m, for the transverse crack heat treated specimens according to the ASTM E-647 (ΔK decreasing). Moreover, analyzing the Paris region, a comparison between heat treated specimens and non heat-treated ones, reveals that the heat treatment doesn't affect significantly the long crack behavior, that shows comparable values with those of wrought counterparts. This means that process induced defects don't influence the FCG behavior as they do for fatigue life. The results in term of crack growth rate against stress intensity factor range are reported in Figure 8.
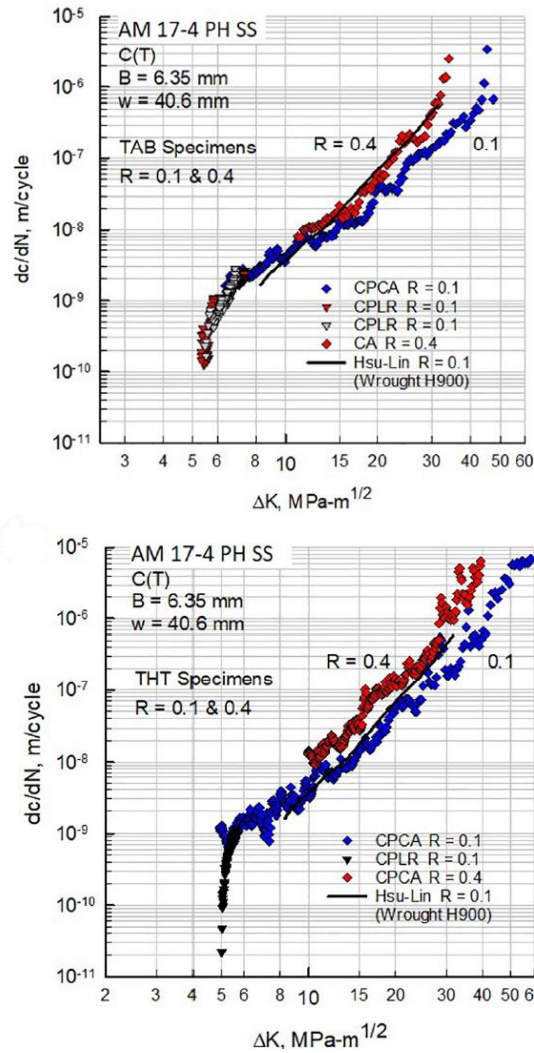
Figure 8: Fatigue crack growth rate experimental data of LB-PBF 17-4 PH SS with transverse notch as-built (left) and CA-H1050 heat-treated (right), compared to wrought 17-4 PH SS subjected to H900 heat treatment. Figure taken from [16].

All the aspects reported in these papers highlight how the presence of defects typical of AM production affects the mechanical properties of AM 17-4 PH SS. The entity of this effect was studied in 2020 by Romano et al.[17] in terms of fatigue life and fracture behavior. The set of studied specimens consisted in 10 net-shape uniaxial fatigue specimens, 10 oversized uniaxial specimens machined to the net-shape dimensions and 8 fatigue crack growth specimens (SE(B) in particular). All the parts were built in the same job, under Nitrogen atmosphere, and then subjected to CA-H1025 heat treatment, consisting in solution heat treating at 1050 °C for 30 minutes, air cooling to room

temperature and then heat treating at 552 °C for 4 hours followed by air cooling to room temperature. After that, the influence of microstructure on the fatigue performance of the material is eliminated. To identify the amount and morphology of internal defects, an analysis of the polished sections has been made: the net shape specimens highlighted the presence of relatively large sub-surface pores (the largest had a √area of 55µm), while for the shallow and deep machined specimens, the presence of large pores close to the surface was eliminated (Figure 9). The number and size of remaining pores were the same for all the sets of specimens. Regarding the surface condition, the net shape specimens revealed deep valleys due to the surface roughness (max valley depth of 65 µm), that negatively affects the fatigue performance.
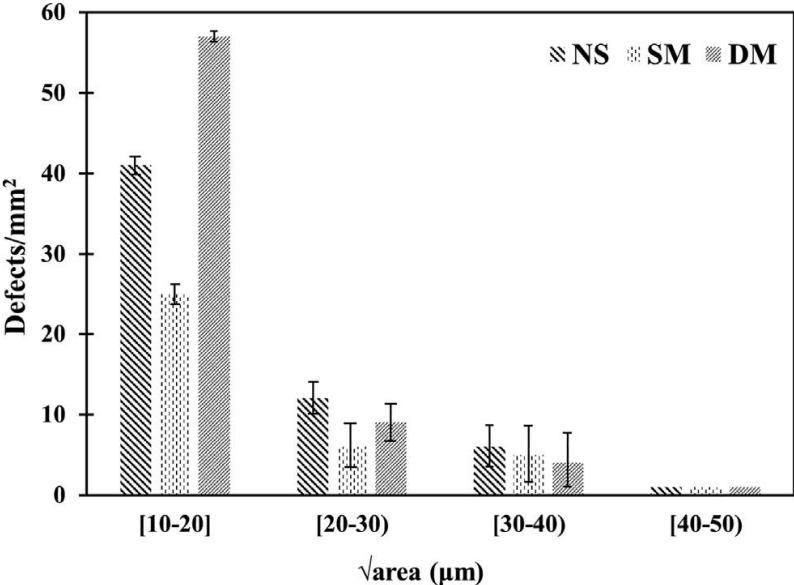
Figure 9: *Comparison between porosity size distribution obtained from polished sections of net-shape, shallow-machined and deep-machined uniaxial fatigue specimens. Figure taken from* [18].

To evaluate the fatigue and fracture performance, axial fatigue tests and four point bending tests were respectively performed. The fatigue life results revealed a significant increase of 200-300 MPa of the fatigue strength for the machined specimens. This has to be ascribed to the failure mechanism: for the net shape samples, the surface cracks due to the surface roughness determined a lower fatigue resistance, while for the machined, cracks were initiated from sub-surface pores of 20-30 µm. Consequently, increasing the machining depth to more than 0.5 mm has no effects on

fatigue life, and according to this paper, the optimal depth for the machining is 200 µm. The fatigue crack growth behavior was studied with ΔK decreasing tests and then analyzed by fitting the experimental data with the NASGRO equation. The obtained threshold is 4.06 MPa√m. Both fatigue and fracture data are reported in Figure 10:
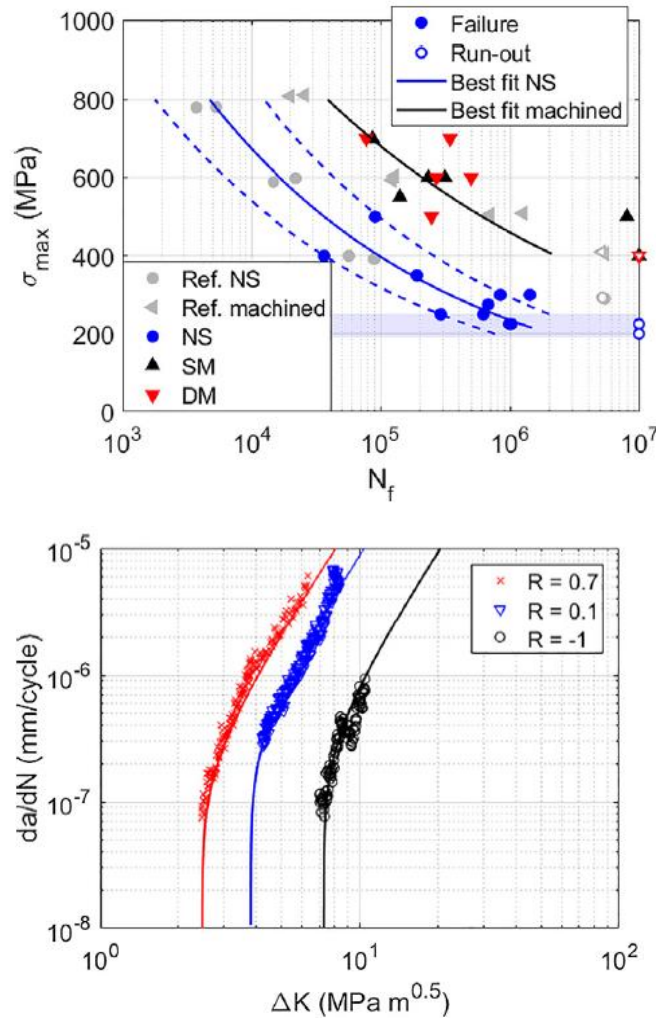
Figure 10: *Experimental data and best-fitting curves of 17-4 PH SS, for uniaxial fatigue tests and fatigue crack growth tests. Figure taken from* [18].

2 Materials and Methods

2.1 Materials and specimen preparation

In this study, Argon-atomized 17-4 PH SS powder was used to fabricate specimens using LB-PBF system (EOS M290). The chemical composition of the pre-alloyed powder is reported in **Errore. L'origine riferimento non è stata trovata.**. To understand the effect of thickness and surface conditions on the FCG behavior, a total

of 32 blocks with different geometries were vertically built. The employed process parameters were recommended by EOS and are listed in **Errore. L'origine riferimento non è stata trovata.**. The job design and the different thicknesses of the blocks are reported respectively in **Errore. L'origine riferimento non è stata trovata.** and **Errore. L'origine riferimento non è stata trovata.**.

Table 3

Number of specimens produced for each geometry, considering the different thicknesses and surface conditions.

Specimens	Thickness [mm]	Surface condition
4	5.0	AB
4	5.7	AB
4	6.4	AB
4	7.1	AB
4	5+2*	Machined
4	5.7+2*	Machined
4	6.4+2*	Machined
4	7.1+2*	Machined

*Machined specimens are oversized by about 2 mm for post-finishing operations

Table 4

Chemical composition of 17-4 PH SS.

Elements	Al	Sn	S	Si	P	O	N	Nb+Ta
Wt %	0.01	<0.01	0.002	0.41	0.005	0.04	0.007	0.28
Elements	**Ni**	**Mo**	**Mn**	**Fe**	**Cu**	**Co**	**Cr**	**C**
Wt %	4.38	<0.01	0.39	Bal.	3.31	0.01	15.76	0.02
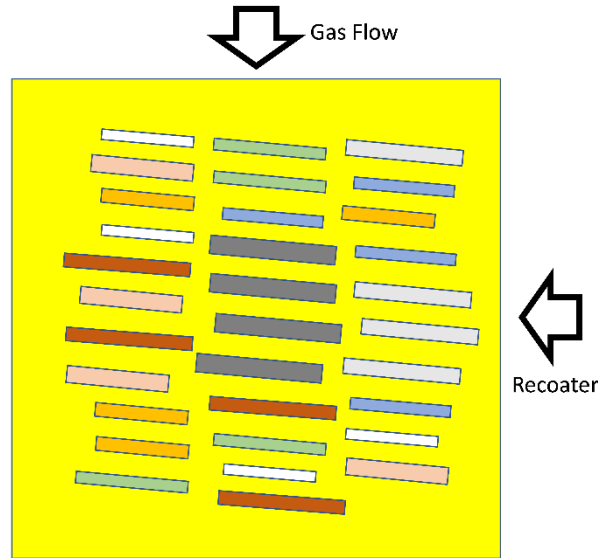
Figure 11: *Position and orientation of the specimens during the L-PBF process.*

The balance between elements permits to have a better mix of properties and an easier process management. Regarding ferritizing elements, Chromium is the main element in stainless steels, and gives resistance to corrosion, Molybdenum enhances the mechanical and corrosion properties, Silicon is typically added to improve the high temperature behavior. Regarding the austenitizing elements, Nickel reduces the corrosion rate and forms intermetallic precipitates, Copper is useful in acid environments and for precipitates, Manganese improves ductility at high temperature, and Carbon and Nitrogen are used to enhance mechanical resistance and hardness, at the expense of toughness. Other elements such as Aluminum, Niobium, and Tantalum are typical of PH SS, as they form strengthening precipitates. All this combination of properties is well described considering the equivalent Chromium and Nickel:

$$Cr_{eq} = \%Cr + 1.5 \cdot \%Si + \%Mo = 16.39$$

$$Ni_{eq} = \%Ni + 30 \cdot (\%C + \%N) + 0.5 \cdot (\%Mn + \%Cu + \%Co) = 7.05$$

Table 5

Process parameters of the L-PBF process.

Laser power [W]	Scanning speed [mm/s]	Hatching distance [µm]	Stripe width [µm]	Layer thickness [µm]
220	755.5	100	100	40

With the obtained values, the material can be characterized using the Shaeffler-Delong diagram (Figure 12: Shaeffler-Delong diagram used to characterize Stainless Steel microstructure as a function of equivalent Chromium and NickelFigure 12) and a prevalent martensitic phase is expected, with a minimum part of ferritic and austenitic phases present, that will be further reduced after the heat treatment.
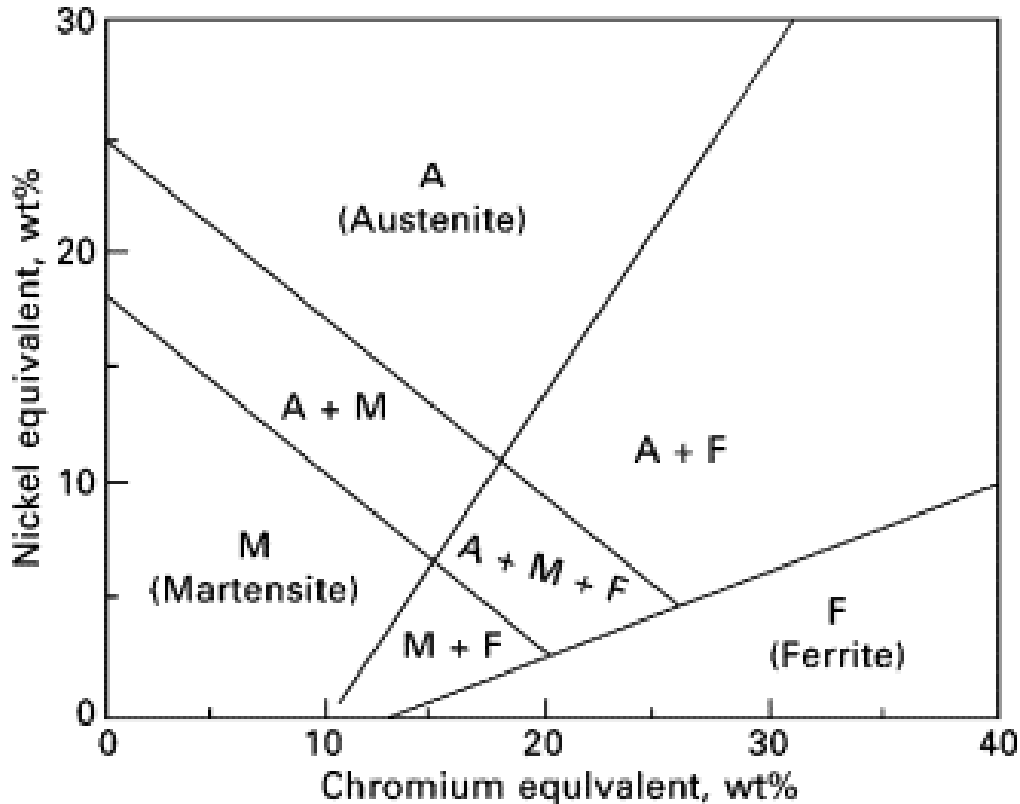
Figure 12: Shaeffler-Delong diagram used to characterize Stainless Steel microstructure as a function of equivalent Chromium and Nickel. Figure taken from [19].

All the samples were then heat treated with a standard procedure of three steps:

- Stress relieving, at 700 °C for 1 hour followed by furnace cooling
- Solution treating, at 1050 °C for 0.5 hours followed by air cooling
- Aging, at 552 °C for 4 hours followed by air cooling

Step 2 and step 3 combined are known as CA-H1025 heat treatment, which permits to go in the austenitic field, then quenching to obtain fine martensite grains, and finally, the precipitation hardening, characterized by the formation of fine strengthening precipitates.

A scheme of the heat treatment is reported in Figure 13:
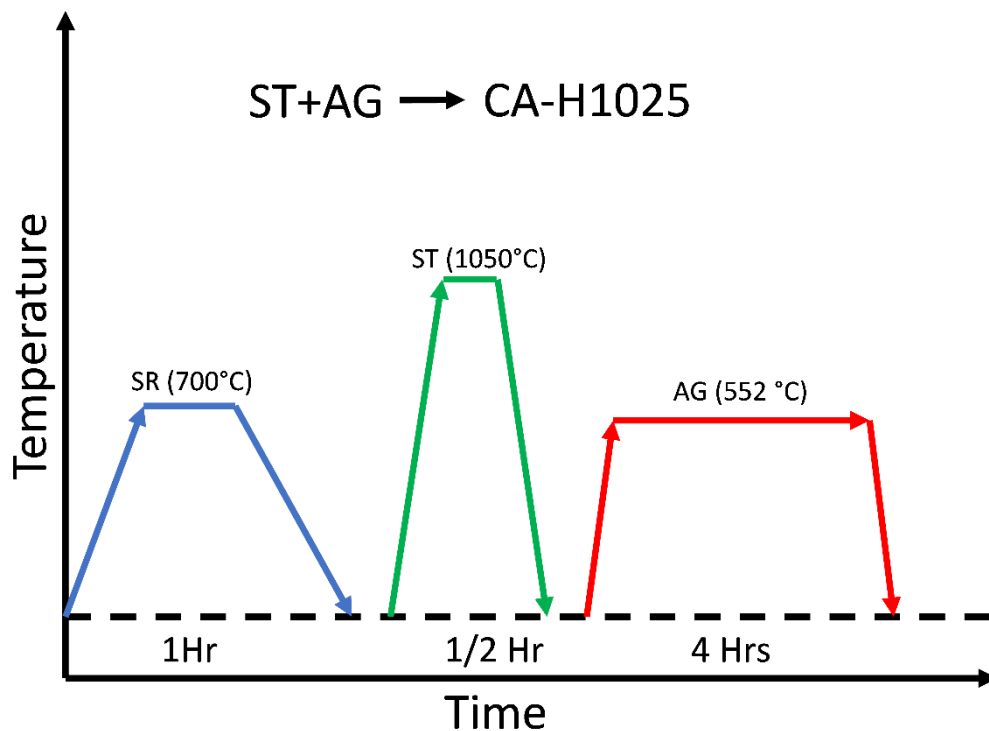
Figure 13: Plot of the temperature versus time characterizing the heat treatment.

After the thermal treatment, the oversized samples were machined to obtain the same geometry as the corresponding as built counterparts.

Finally, the blocks were machined, with respect of the ASTM E-647, into the final configuration of CT specimen. The geometry of the entire experimental apparatus is defined in the method as a function of thickness (B) and width (W). It is also recommended for the thickness to be in the range of $W/20 \leq B \leq W/4$. It is important to underline that all the limits are based on specimen buckling and through-thickness crack-curvature considerations, mostly from empirical data. The geometry suggested by the method is reported in Figure 14:
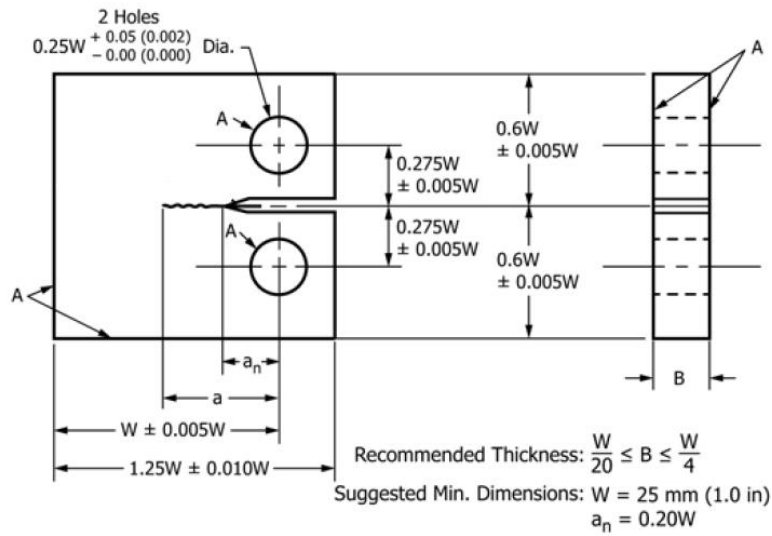
Figure 14: CT specimen geometry for fatigue crack growth testing, according to the ASTM E-647. Figure taken from [11].

Regarding the notch, the method doesn't suggest a unique solution (Figure 15), but it depends on the tested material. In the case of high-strength steel, the notch has to be obtained with electro-discharge machining (EDM) with a notch root radius $\rho < 0.25$ mm to facilitate the pre-cracking phase.
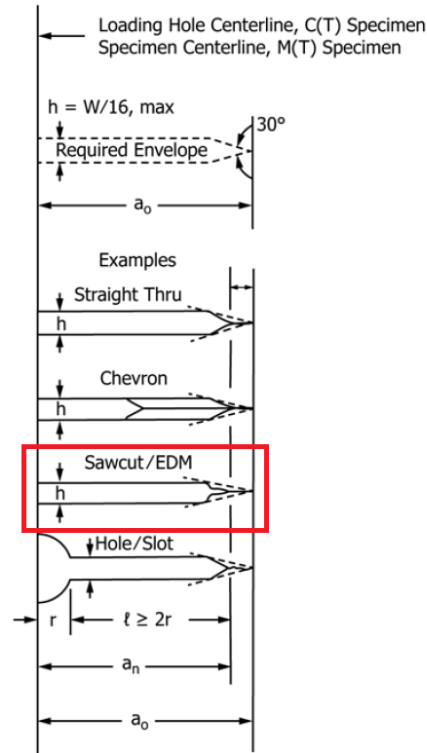
Figure 15: *Notches suggested by ASTM E647, as a function of material and machining technique. Figure taken from* [11].

In this study, two different geometries were tested and analyzed, both in the machined and as built condition, for a total of 9 specimens: 2 L1MC, 3 L1AB, 2 L3MC and 2 L3AB. The sample geometries are reported in Figure 16:
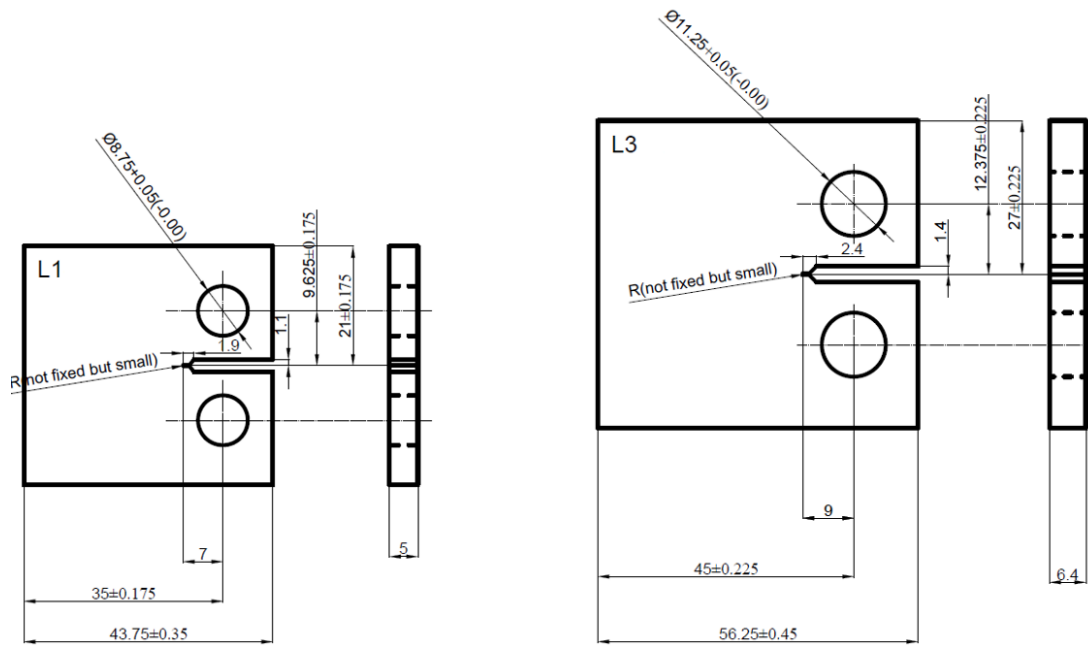
Figure 16: Specimen geometries in accordance with the standard ASTM E-647. Dimensions are in millimeters.
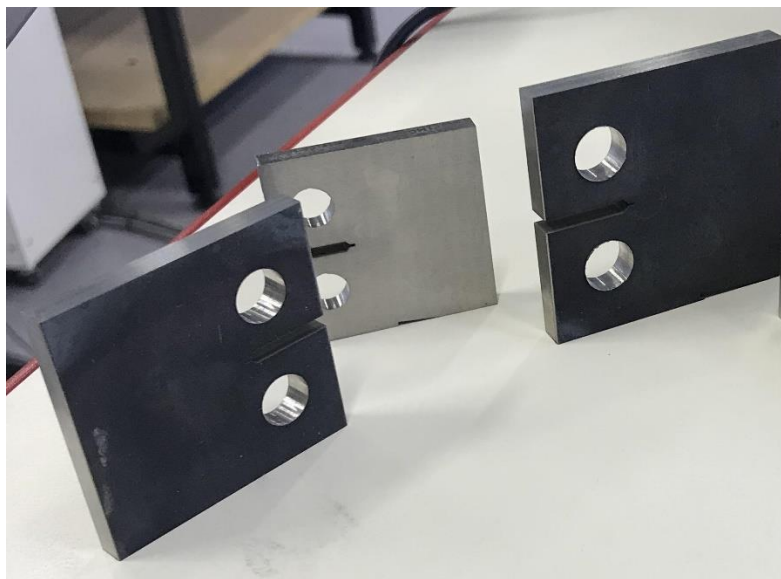
Figure 17: Example of CT specimens used for FCG testing, with different geometries and surface conditions.

2.2 Test

This study is carried out according to the ASTM E647, the standard method for measurements of fatigue crack growth rates. This method expresses the results in term

of the crack-tip stress-intensity factor range (ΔK) defined by the Linear Elastic Fracture Mechanics Theory. The main output is the expression of da/dN as a function of ΔK, which can be utilized in the design and evaluation of engineering structures. The method involves cyclic loading of notched specimens which have been pre-cracked in fatigue. The focus will be on the behavior of long cracks, which are considered so when the transition from the initiation to the propagation stage of fatigue is complete. The purposes of the method are to establish:

- the influence of fatigue growth on the life of components subjected to cycling loading
- material inspection criteria and inspection requirements for damage tolerant approach
- effects of metallurgical, fabrication, environmental and loading variables on fatigue crack growth

2.2.1 Pre-crack phase

The importance of pre-cracking is to provide a sharpened fatigue crack of adequate size and straightness, to eliminate the effect of pre-crack load history on the subsequent crack growth rate data. For the tested specimens, the standard suggested a minimum pre-crack with an extension not shorter than h Figure 15. Furthermore, the final K_{max} during pre-cracking shall not exceed the initial K_{max} for which test data are to be obtained; however, higher initial loads to facilitate the pre-crack phase are allowed with the condition that the load is decreased in a step-wise manner, with a reduction for any steps not greater than 20%, up to the final K_{max} to be used during the test. Another constraint for this pre-cracking technique is to have a crack size increment per step of at least $(3/\pi)(K^I_{max}/\sigma_{YS})^2$, being K^I_{max} the final K_{max} value during the previous step.

The first samples tested made it possible to estimate a suitable starting value of ΔK, which permits to have a crack in a reasonable time (in terms of number of cycles); a value of 25 MPa√m has been found to be a reasonable compromise. Starting from this

value, the correspondent load to apply can be evaluated using the equation suggested by the method, as follows:

$$\Delta K = \frac{\Delta P}{B \sqrt{W}} \frac{(2+\alpha)}{(1-\alpha)} (0.886 + 4.64\alpha - 13.32\alpha^2 + 14.72\alpha^3 - 5.6\alpha^4) \qquad (2.1)$$

Therefore, after the arbitrary choice crack sizes increment fulfilling the requirement stated in the above, and knowing that the load ratio is R=0.1, all the different pre-cracking steps were defined as reported in Table 6:

Table 6

Example of calculation of pre-cracking steps according to ASTM E647 criteria.

Step	1	2	3	4	5
L_{max} [N]	6000	5000	4000	3200	2600
L_{min} [N]	600	500	400	320	260
B [mm]	5	5	5	5	5
W [mm]	35	35	35	35	35
a_i [mm]	7	7,7	8,2	8,6	8,95
a_f [mm]	7,7	8,2	8,6	8,95	9,2
ΔK_i [MPa m$^{0.5}$]	24,7	21,8	18,2	15	12,5
ΔK_f [MPa m$^{0.5}$]	26,2	22,7	18,7	15,3	12,7
Δa [mm]	0,7	0,5	0,4	0,35	0,25

For every different set, the first specimen to be tested was always a MC one, because of the possibility to check the crack length, either measuring it with a caliber directly on the specimen, or digitally at the microscope. This operation allows also to verify the data obtained with the non-visual technique employed for measuring the crack length (back face strain gauge, described in detail in 2.2.3), as the method suggests to do.
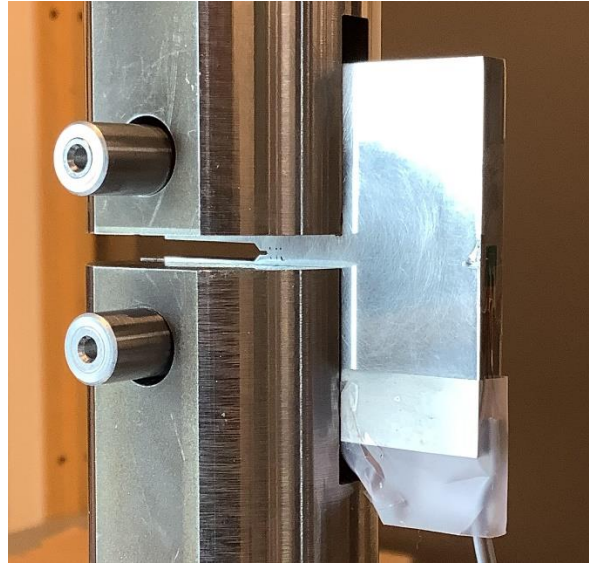
Figure 18: *Typical pre-cracking phase configuration.*

The procedure described requires a certain degree of expertise, because of the strict constraints imposed by the standard. The first MC specimen is also used as a guide to achieve an estimation of the number of cycles needed for every step (to be used for the as-built samples, due to difficulties in detecting the crack through visual measurements). The steps for pre-crack procedure are reported in tables as the following one:

Table 7

Pre-cracking steps for L1MC-2 specimen.

	L1MC-2		
Step	Lmax [N]	Frequency [Hz]	N
1	6000	40	28000
2	5000	40	7000
3	4000	40	8800
4	3200	40	14000
5	2600	40	154000
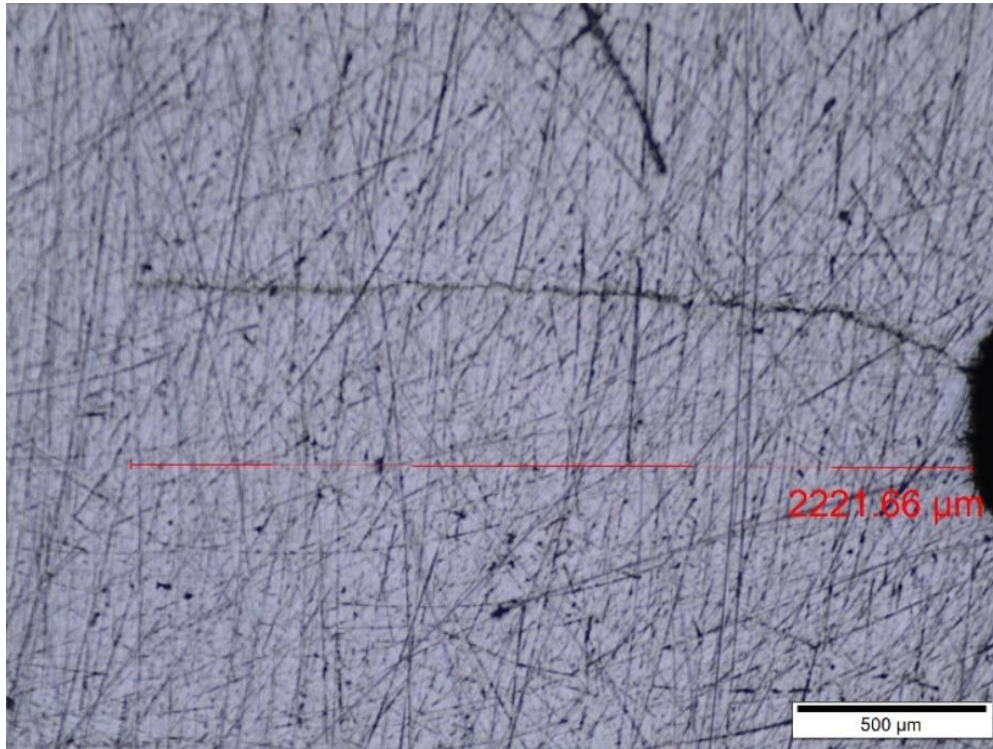
Figure 19: *Visual size measurement at the end of the pre-cracking phase for an L1MC specimen.*

The pre-cracking phase of the as built specimens is more complicated and challenging, due to the impossibility to check visually the crack length, and for obvious reasons, it is not possible to polish the interested area. In this case, a first attempt was made with a visual check at the microscope, with unsatisfactory results. Even if the presence of a crack is somehow feasible, an exact measurement is almost impossible.
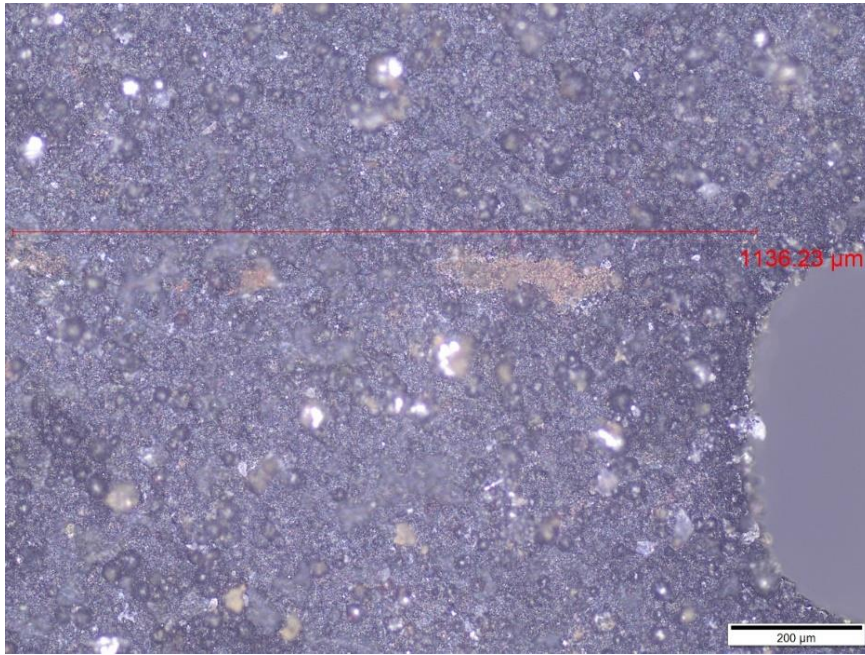
Figure 20: *Crack detection on a L1AB specimen with a visual technique. The crack size reported is referred to the corresponding measurement with a non-visual technique.*

For this reason, for the AB specimens, the pre-cracking phase is based on the MC specimens results and on the non-visual technique measurement. The visual check is postponed at the end of the test, evaluating the beachmarks present in the fracture surfaces with a procedure described in 2.2.4. In any case, after the data analysis and visual check, it can be said that the AB behavior in the pre-cracking is approximately the same as the MC ones.

2.2.2 Constant Amplitude

In this study, tests were conducted with constant force amplitude procedure. This test procedure is well suited for fatigue crack growth rates above 10^{-8} m/cycles, corresponding to regime II of the FCG curves. The standard suggests to test each specimen at a constant force range (ΔP) and a fixed set of loading variables (stress ratio and frequency). Consequently, all the tests were conducted under the same load ratio R=0.1 and frequency f=20 Hz, while the load range was determined as a function of the geometry, and was calculated as it was an additional step of the pre-cracking (reducing of about 20% the maximum load of the last pre-cracking step and not considering the first increment of the crack length that may be affected by crack retardation induced by the previous load step at higher load value). It is worth noting that such a procedure results in a ΔK Increasing procedure; indeed, keeping constant the load, ΔK will increase with increasing the crack length during the test. For every specimen, at the end of the test it is possible to build a table like the following:

Table 8

Example of test process parameters for an L1MC specimen.

L1MC-2			
R	**L_{max} [N]**	**Frequency [Hz]**	**N_f**
0.1	2100	20	1031350

After the test, the standard demands that some conditions are met to consider the test valid (respected by all the specimens of this study), based on the geometrical parameters of the crack front while growing. Referring to the CT specimen, two criteria must be satisfied:

- Crack size symmetry: crack size measurement should be made on both sides of the specimen. This requirement is complicated to be verified if a non-visual measurement technique is used, and it is recommended to not stop the test if not necessary. For these reasons, the method suggests evaluating the crack size symmetry with a visual check of the fracture surface.

Figure 21: Crack size symmetry validation for an L1MC specimen.

- Crack deviation: if the crack deviates more than ±20° from the plane of symmetry over a distance of 0.1W or greater, the data are invalid.
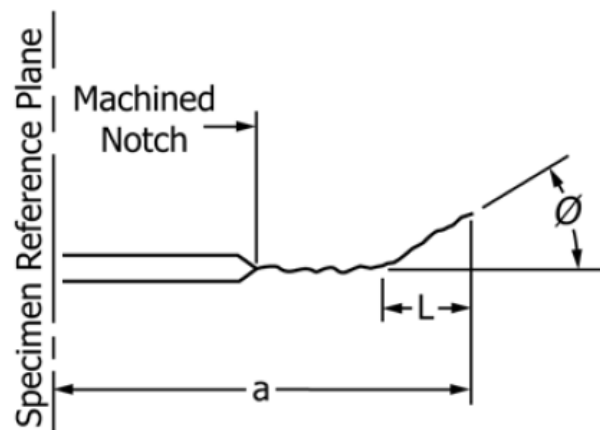
Valid if Ø ≤ 10°
Report if 10° < Ø ≤ 20°
Invalid if Ø > 20° for L ≥ 0.1W

Figure 22: Representation of crack deviation constraint, according to ASTM E-647

[11].

According to the standard, the measurement of crack size has to be made as a function of elapsed cycles. In this study, the back face strain gauge technique was used, and this permits to build a table like the following:

Table 9

Parameter report after the constant amplitude testing procedure.

a_i	N_i
a_1	N_1
a_2	N_2
…	…
a_n	N_n

In order to obtain an adequate plot, the crack size measurement should be made at intervals such that da/dN data are nearly evenly distributed with respect to ΔK. For the CT specimen, the suggested intervals are:

$$\Delta a \leq 0.04 \text{ W for } 0.25 \leq a/W \leq 0.4$$

$$\Delta a \leq 0.02 \text{ W for } 0.4 \leq a/W \leq 0.6$$

$$\Delta a \leq 0.001 \text{ W for } a/W \geq 0.6$$

However, stricter limits have been applied, and the result is reported in Figure 23:

$$\Delta a \leq 0.015 \text{ W for } 0.25 \leq a/W \leq 0.4$$

$$\Delta a \leq 0.01 \text{ W for } 0.4 \leq a/W \leq 0.6$$

$$\Delta a \leq 0.0075 \text{ W for } a/W \geq 0.6$$
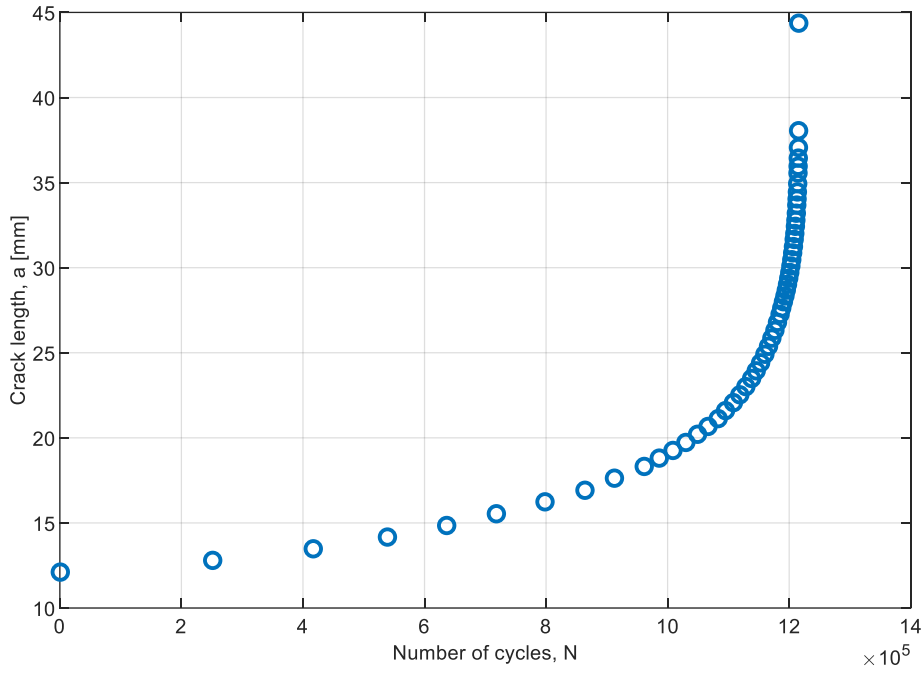
Figure 23: Crack length versus number of cycles plot after the data processing suggested by the standard ASTM E-647.

According to the standard, there are two two methodologies are allowed to calculate the crack growth rate: the secant method and the incremental polynomial method. In this study, the first one has been used, and it consists of the calculation of the slope of the straight line connecting two adjacent data points on the *a* versus *N* curve. Formally, it can be expressed as follows:

$$(\frac{da}{dN})_{\bar{a}} = (a_{i+1} - a_i)/(N_{i+1} - N_i) \tag{2.2}$$

As it can be seen from the previous formula, the computed crack growth rate is an average rate over the (a_{i+1}-a_i) increment, and for this reason, the average crack size $\bar{a}$=(a_{i+1}-a_i)/2 is used to calculate ΔK.

The last step in the data analysis regards the determination of the stress intensity factor range. For the CT specimen, the expression to be used is the following:

$$\Delta K = \frac{\Delta P}{B \sqrt{W}} \frac{(2+\alpha)}{(1-\alpha)} (0.886 + 4.64\alpha - 13.32\alpha^2 + 14.72\alpha^3 - 5.6\alpha^4) \tag{2.3}$$

Where ΔP is constant during the test, B and W are geometrical properties defined in 2.1, and α=a/W is calculated using the average value of crack size a for every adjacent data points.

Once collected the crack size *a*, the number of cycles *N*, and calculated the crack growth rate d*a*/d*N* and the stress intensity factor range ΔK, it is possible to build a table like the following:

Table 10

Structure of parameter report after the data processing.

a_i	N_i	d*a*/d*N*	ΔK_{Ii}
a_1	N_1	$(da/dN)_1$	ΔK_{I1}
a_2	N_2	$(da/dN)_2$	ΔK_{I2}
…	…	…	…
a_n	N_n	$(da/dN)_n$	ΔK_{In}

According to the method, d*a*/d*N* as a function of ΔK shall be plotted using log-log coordinates:
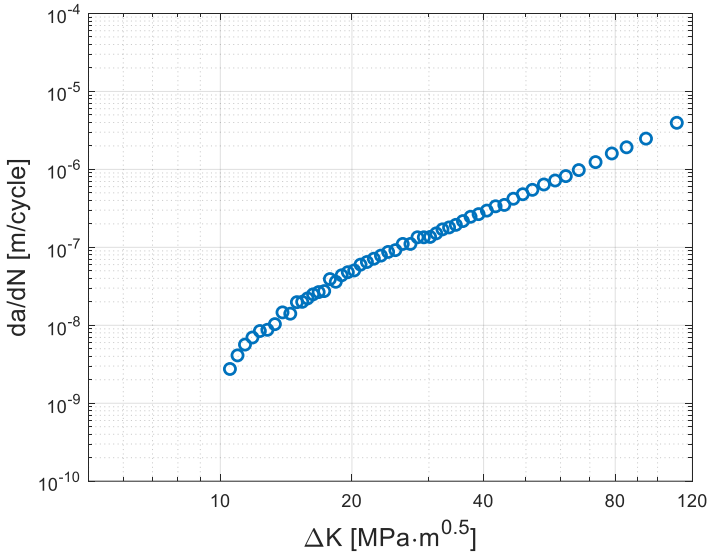
Figure 24: *Crack growth rate data points as a function of the stress intensity factor range in log-log coordinates, resulting from the test data processing.*

Finally, region II of the fatigue crack growth curves can be characterized by calculating the Paris law coefficients using a non-linear regression of the data from the previous plot.

$$Paris\ Law: \quad \frac{da}{dN} = C \cdot \Delta K_I{}^m \tag{2.4}$$
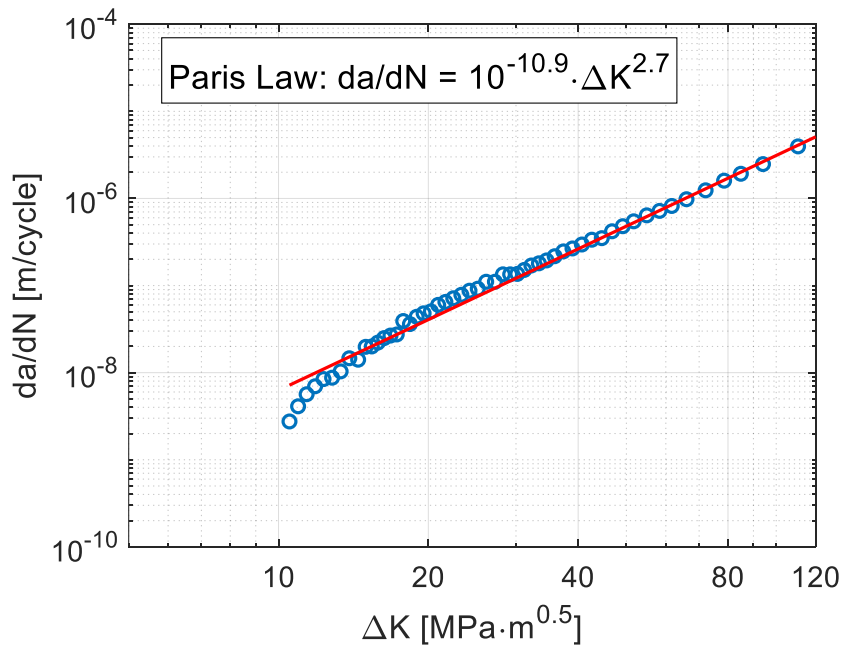
Figure 25: *Non-linear regression of the processed test data points, resulting in the determination of Paris Law coefficients C and m.*

2.2.3 Back face strain gauges

Strain gauges are devices used to measure the strain of the materials under mechanical or thermal loads, and for their high precision grade, they are used typically in laboratory activities. Strain gauges are made up of fine electric resistance wire, an electrical insulation base, and the gauge leads.
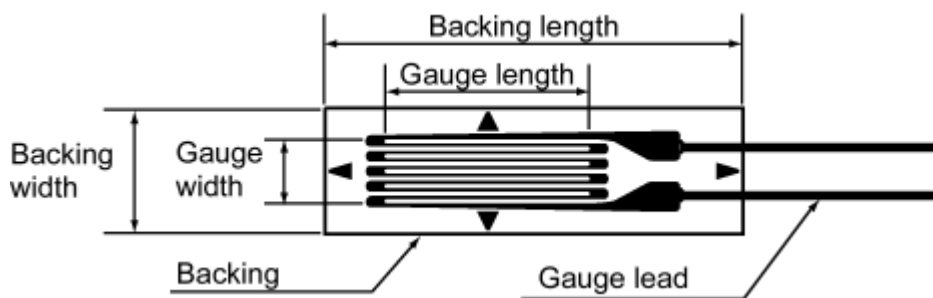
Figure 26: *Strain gauge representation and definition of the geometrical parameters. Figure taken from* [20].

When strain is generated in a specimen, and the strain gauge is attached, the strain is relayed via the gauge base to the resistance wire. As a result, the fine wire experiences

a variation in electrical resistance, that is exactly proportional to the strain according to the following equation:

$$\varepsilon = \frac{\Delta L}{L} = \frac{\frac{\Delta R}{R}}{K}$$

(2.5)

Where: ε = strain measured

L = original length of the material

ΔL = change in length

R = gauge resistance

ΔR = resistance change due to strain

K = gauge factor

For the standard, it is allowed to monitor the crack size by measuring strains at the back face (with respect to the notch), at a location along the crack plane. The constraint is that the ratio of strain gauge length, l, to specimen width, W, falls within $0 \leq l/W \leq 0.05$.
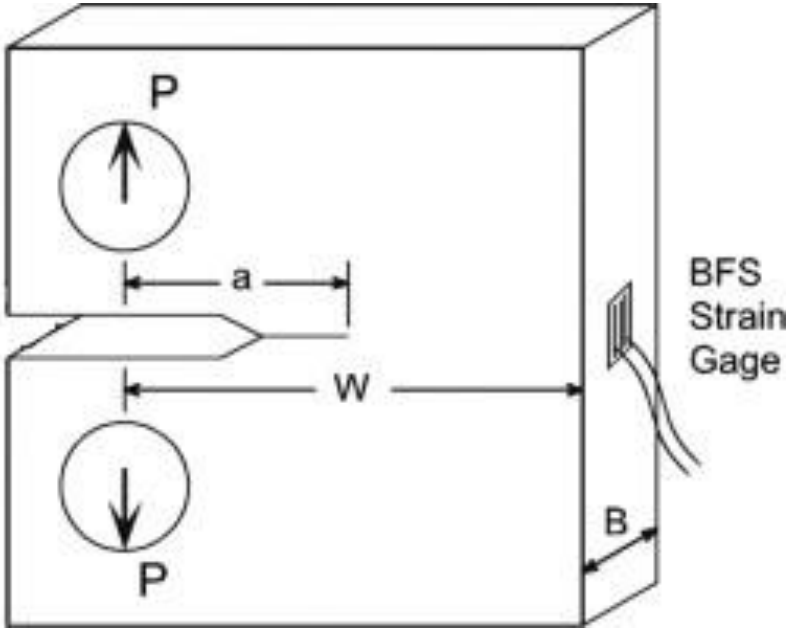
Figure 27: Representation of CT specimens and Back Face Strain Gauge application. Figure taken from [21].

'FLAB-1-23-1LJC-F' model strain gauges by Tokyo Measurement Instruments Lab, were used in the tests. The strain gauge parameters are reported in Table 11, according to the datasheet available on the supplier website [20]:

Table 11

Geometrical parameters of the strain gauges used for FCG testing, according to Tokyo Measurement Instruments Lab [20].

Gauge size [mm]		Backing size [mm]		Resistance [Ω]	Lead wire length [m]
Length	Width	Length	Width		
1	1.3	5	2.5	120	1

Considering the cyclic load applied and the position of the strain gauge, due to the compressive stress in the back face, the measured strain is negative. The correspondence between these two parameters is reported in figure:
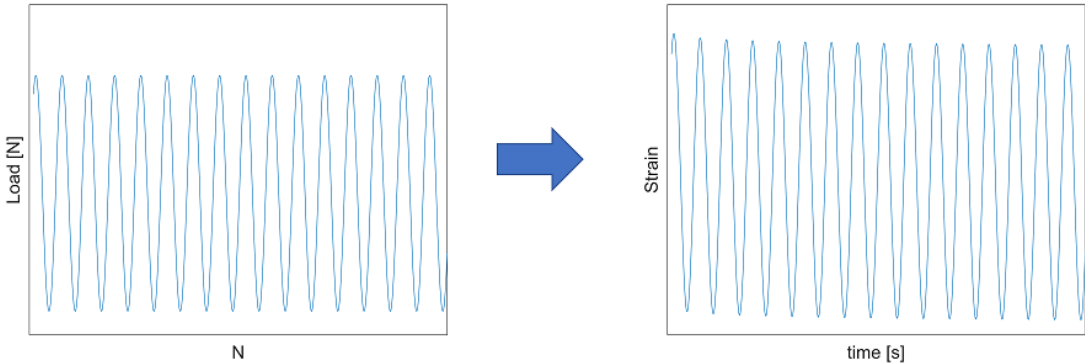
Figure 28: Schematic representation of the applied load during FCG tests and the corresponding strain gauge output.

Catman software was used to collect and analyze the output data from the strain gauge. In particular, both the measured strain and the number of cycles the data collected have been recorded with a sample rate of 2400 Hz to lose the less amount of data as possible and to properly catch the sinusoidal law describing the strain that has a frequency equal to that of the load during the test.

The standard provides the equation to calculate the crack size starting from the strain value:

$$a = W(N_0 + N_1 U + N_2 U^2 + N_3 U^3 + N_4 U^4 + N_5 U^5) \qquad (2.6)$$

Where: $U = 1/(A^{1/2}+1)$

$A = \left| \varepsilon EBW/P \right|$

$N_0 = 1.0033$

$N_1 = -2.35$

$N_2 = 1.3694$

$N_3 = -15.294$

$N_4 = 63.182$

$N_5 = -74.42$

It is important to underline that the equation is valid for every value of the load, and consequently on every point of the cycle. However, the implemented equation in the software contains the maximum nominal load applied during the test and the corresponding maximum absolute value of the strain. This choice has been made in order to minimize the relative error that may affect the strain measure and due to signal delays between the load and the strain ones. The displayed data during the test are in Figure 29:
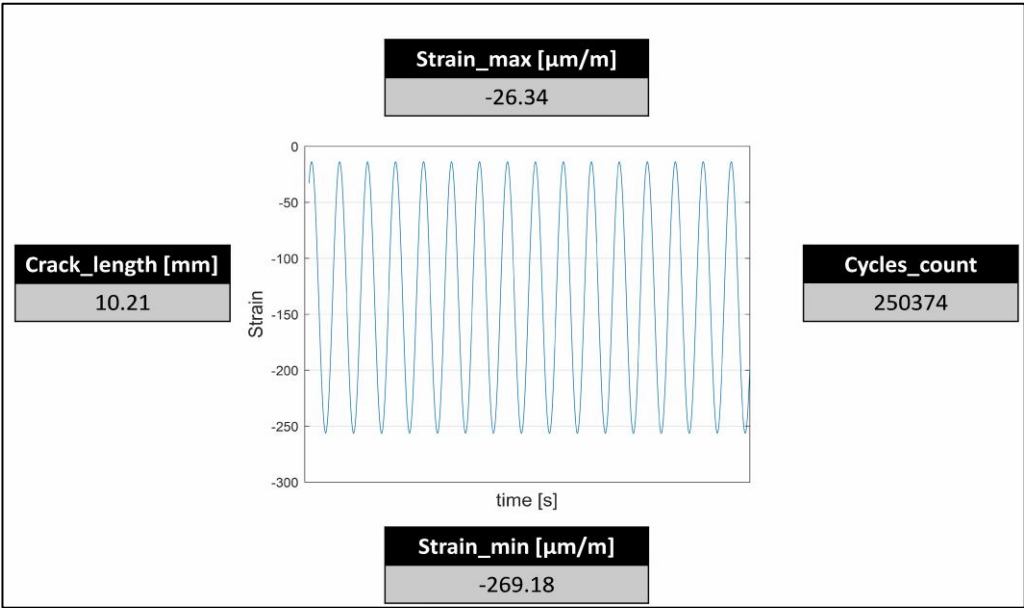
Figure 29: *Example of Catman displayed output during a FCG test.*
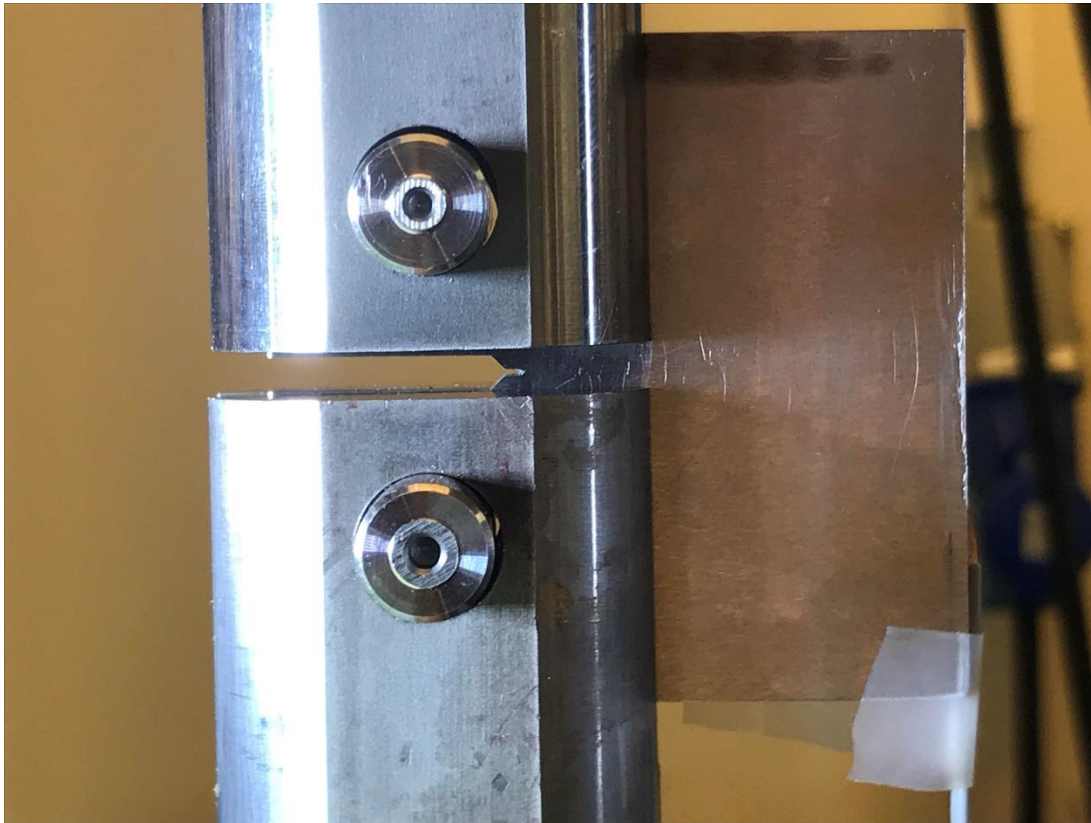
Figure 30: Example of the typical FCG test configuration.

2.2.4 Beach marks

In the standard it is reported several times the importance of avoiding test interruption, and if it's not possible, the downtime must be as short as possible. The constraint imposed by the standard for the validation of the test in presence of interruptions, is the correspondence between the crack growth rates before and after the stop. Another requirement of the method is to verify with visual techniques the crack size measurements made with non-visual techniques, as in the case of this study. In addition, the AB specimens are characterized by an intrinsic difficulty in monitoring the crack size due to the surface condition. The solution adopted in the tests of this study is to exploit the beach marks. As reported by Ermakova et al. [22] bechmarking should be carried out at different intervals throughout the tests to cross-check the accuracy of the estimated crack length from the backface strain gauge technique. In this method, the frequency and the maximum cyclic fatigue load are decreased for a limited number of cycles to introduce thin marks on the fracture surface, so called

beachmarks. In order to apply the beachmarking tehniques, the loading conditions are changed as follows: the frequency is decreased from 20 Hz to 4 Hz, the load ratio is increased from R=0.1 to R=0.125, keeping constant the minimum load (as a consequence, the maximum load will decrease). This procedure was performed two to three times, to introduce multiple beachmarks in addition to the one deriving from the pre-cracking phase for the validation of the calibration curves.

Table 12

Test parameters for L1MC.

Lmax [N]	R	F [Hz]	N
2100	0.1	20	250000
1680	0.125	4	6000
2100	0.1	20	500000
1680	0.125	4	6000
2100	0.1	20	170000
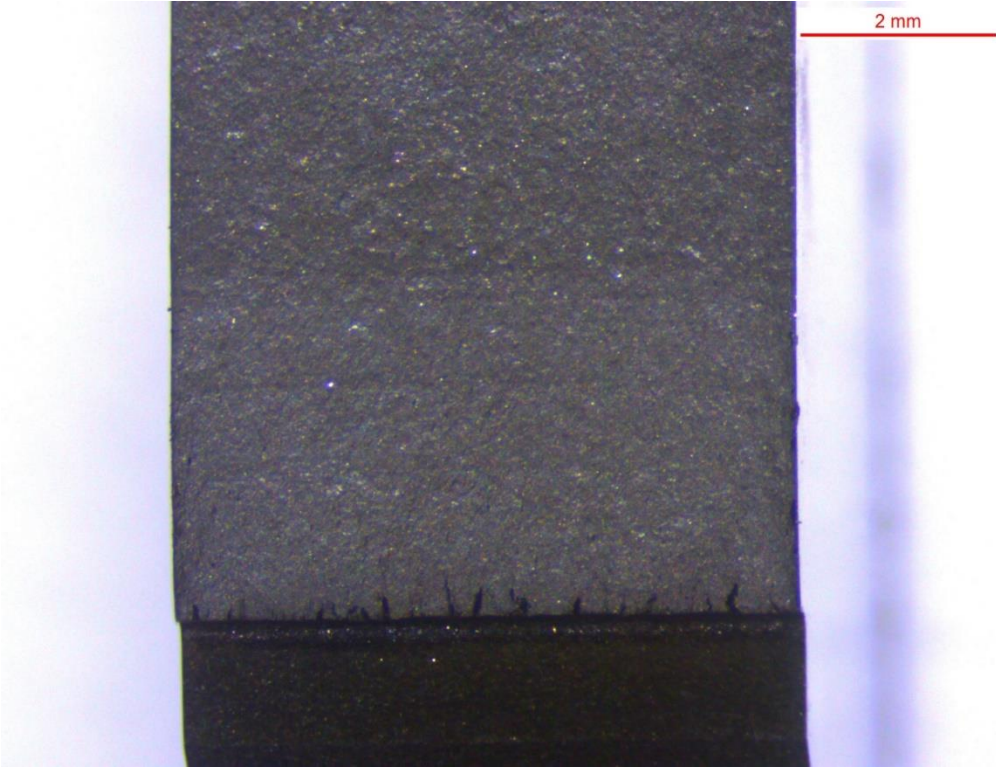
Figure 31: *Beachmarks on fracture surface of L3MC specimen.*

The importance of this technique lies in the possibility of automating the process, but its effectiveness is strongly dependent on the material and the beachmarking loading conditions. For this reason, for some specimens it was not possible to detect all the BMs on the fracture surface. Consequently, through the different tests the method has been varied, in terms of position (number of cycles of beachmarking) and BMs dimension (increasing the number of cycles). Despite these issues, the technique produced satisfactory results, with at least 2 BMs measured on the crack surface, and a high accuracy, with a maximum different between visual and non-visual measurements of 0.1 mm, in accordance with the standard constraints.
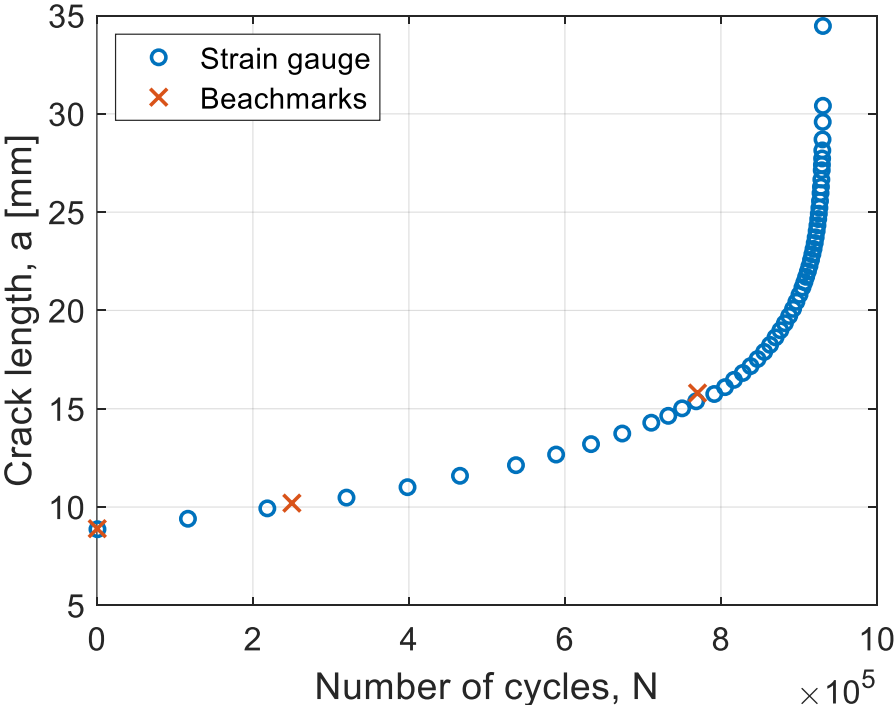
Figure 32: L1AB crack length versus number of cycles plot obtained with back-face strain gauge technique and validation through beachmarks measurement.

3 Results

In general, the FCG behavior is characterized of a certain variability. This can be attributed to the phenomenon intrinsic nature and to all the possible combinations of loading variables (frequency, maximum load, loading ratio, etc…) and material conditions (microstructure, size and amount of defects, surface condition, etc…). In order to allow the most accurate comparison possible between data from different studies, it is a good practice to conduct replicate tests and to report for each one the main variables. In addition to the internal parameters described in detail in Chapter 2, many external parameters can affect the mechanical behavior. In this study, all the tests were conducted in air, at laboratory conditions (temperature of 22 to 23 °C and air pressure).

3.1 Tests reports

L1MC-2

The pre-cracking phase was characterized by a crack curvature that made it difficult to correlate the visual and non-visual measurement techniques. After the test, the correspondence was checked evaluating the through-thickness crack curvature, and no correction was needed.

Table 13

Pre-cracking parameters of L1MC-2 specimen.

	L1MC-2		
Step	Lmax [N]	Frequency [Hz]	N
1	6000	40	28000
2	5000	40	7000
3	4000	40	8800
4	3200	40	14000
5	2600	40	154000

At the end of the pre-cracking phase, the crack size was 8.8 mm, corresponding to a stress intensity factor range of 10 Mpa√m as test initial value. The test was conducted with the parameters reported in Table 14:

Table 14

Test parameters for L1MC-2 specimen.

Lmax [N]	R	F [Hz]	N
2100	0.1	20	380000
1680	0.125	4	6000
2100	0.1	20	645350

The beachmarking procedure was made manually, stopping the test at 380000 cycles and the validation of measurements was positive for both beachmarks (pre-cracking and during test). No other peculiarities were reported for this test. The resulting crack size versus number of cycles plot is reported in Figure 33:

Figure 33: Crack size versus number of cycles plot for the L1MC-2 specimen.

The data from the test were then processed with the secant method in order to obtain the crack growth rate versus stress intensity factor range plot (Figure 34):

Figure 34: Crack growth rate versus stress intensity factor range for the L1MC-2 specimen.

41

L1MC-4

During the first part of the pre-cracking phase, there was no correspondence between visual and non-visual crack size measurement. This can be attributed to the through-thickness crack curvature in the first pre-cracking step. With this consideration, it was preferred to increase the test maximum load from 2100 N (as planned for L1 specimen set) to 2500 N.

Table 15

Pre-cracking parameters of L1MC-4 specimen.

	L1MC-4		
Step	**Lmax [N]**	**Frequency [Hz]**	**N**
1	6000	40	28000
2	5000	40	10000
3	4000	40	8000
4	3200	40	30000
5	2600	40	110000

At the end of the pre-cracking phase, the crack size was 8.1 mm, corresponding to a stress intensity factor range of 11.3 Mpa√m as test initial value. The test was conducted with the parameters reported in Table 16:

Table 16

Test parameters for L1MC-4 specimen.

Lmax [N]	R	F [Hz]	N
2500	0.1	20	694799

Due to the pre-cracking phase criticalities, the beachmarking procedure was avoided during the test. The validation of crack size measurement made with back-face strain gauge was made using the beachmarks from the last two steps of pre-cracking phase, with positive result. The resulting crack size versus number of cycles plot is reported in Figure 35:
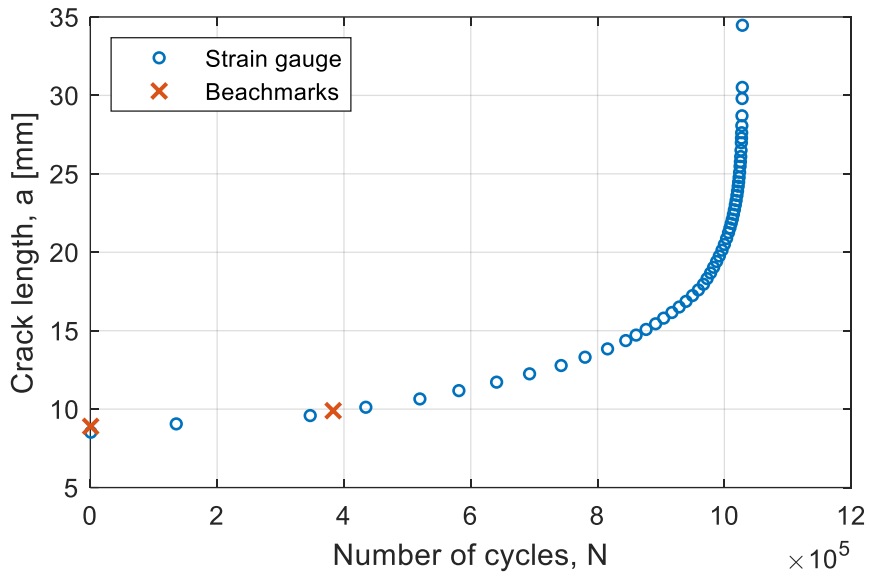
Figure 35: *Crack size versus number of cycles plot for the L1MC-4 specimen.*

The data from the test were then processed with the secant method in order to obtain the crack growth rate versus stress intensity factor range plot (Figure 36):

Figure 36: *Crack growth rate versus stress intensity factor range for the L1MC-4 specimen.*

L1AB-1

The pre-cracking phase was conducted with no interruptions, being the specimen an as-built one and the validation postponed to the end of the test. Due to technical reason, part of the experience data were not recorded and the test was interrupted. It was decided to repeat the pre-cracking procedure to avoid crack retardation phenomenon, and this made it necessary to start the test at a greater crack size. For these reasons, three L1AB specimens was tested, while for the others only two specimens were considered.

Table 17

Pre-cracking parameters of L1AB-1 specimen.

	L1AB-1		
Step	Lmax [N]	Frequency [Hz]	N
1	6000	40	6700
2	5000	40	5000
3	4000	40	5000
4	3200	40	7500
5	2600	40	11600

At the end of the second pre-cracking phase, the crack size was 12.9 mm, corresponding to a stress intensity factor range of 13.5 Mpa√m as test initial value. The test was conducted with the parameters reported in Table 18:

Table 18

Test parameters for L1AB-1 specimen.

Lmax [N]	R	F [Hz]	N
2100	0.1	20	298163

Between the pre-cracking procedures, the test was started and 138000 cycles were recorded at the same loading parameters before the technical issue. In accordance to the standard, these data weren't considered in the following processing. The resulting crack size versus number of cycles plot is reported in Figure 37:

Figure 37: Crack size versus number of cycles plot for the L1AB-1 specimen.

The data from the test were then processed with the secant method in order to obtain the crack growth rate versus stress intensity factor range plot (Figure 38):
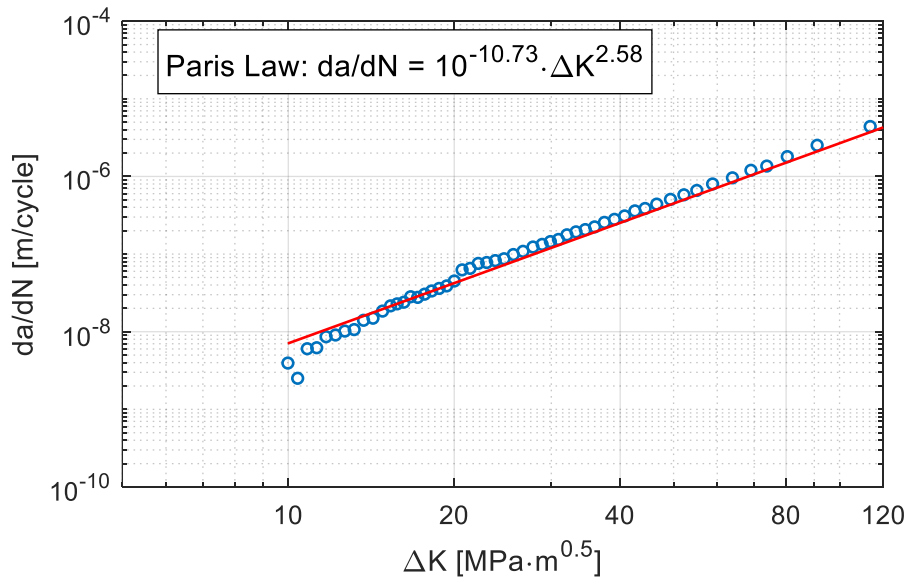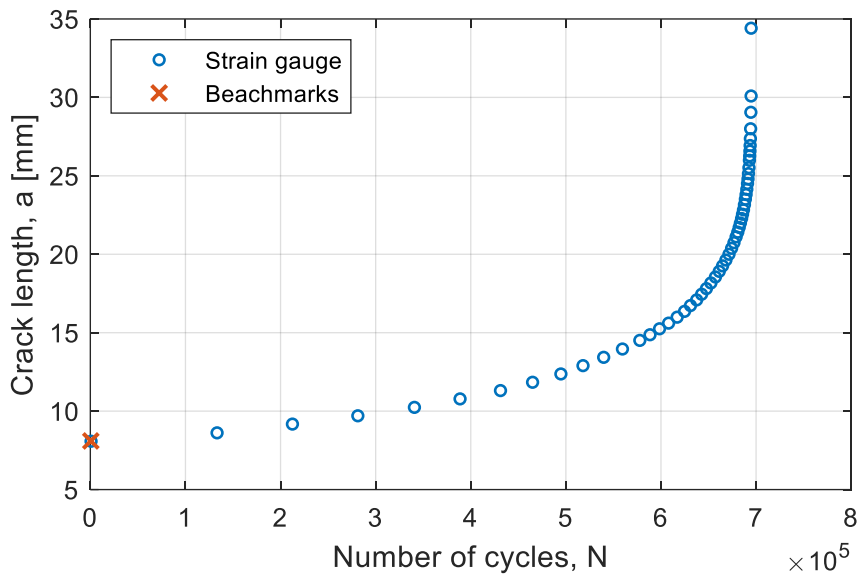

Figure 38: Crack growth rate versus stress intensity factor range for the L1AB-1 specimen.

45

L1AB-2

The pre-cracking phase was made in accordance with the parameters found for the L1MC specimens. Due to the difficulty related to the beachmarking procedure, and with the objective of optimizing the procedure itself, it was decided to increase the number of cycles for each beachmark from 6000 to 10000 cycles.

Table 19

Pre-cracking parameters of L1AB-2 specimen.

	L1AB-2		
Step	Lmax [N]	Frequency [Hz]	N
1	6000	40	28000
2	5000	40	7000
3	4000	40	8000
4	3200	40	44000
5	2600	40	35000

At the end of the second pre-cracking phase, the crack size was 8.9 mm, corresponding to a stress intensity factor range of 10.1 Mpa√m as test initial value. The test was conducted with the parameters reported in Table 20:

Table 20

Test parameters for L1AB-2 specimen.

Lmax [N]	R	F [Hz]	N
2100	0.1	20	250000
1680	0.125	4	10000
2100	0.1	20	250000
1680	0.125	4	10000
2100	0.1	20	250000
1680	0.125	4	10000
2100	0.1	20	150761

In the measurement validation after the test, three out of four beachmarks were clearly visible on the fracture surface.

The resulting crack size versus number of cycles plot is reported in Figure 39:

Figure 39: Crack size versus number of cycles plot for the L1AB-2 specimen

The data from the test were then processed with the secant method in order to obtain the crack growth rate versus stress intensity factor range plot (Figure 40):
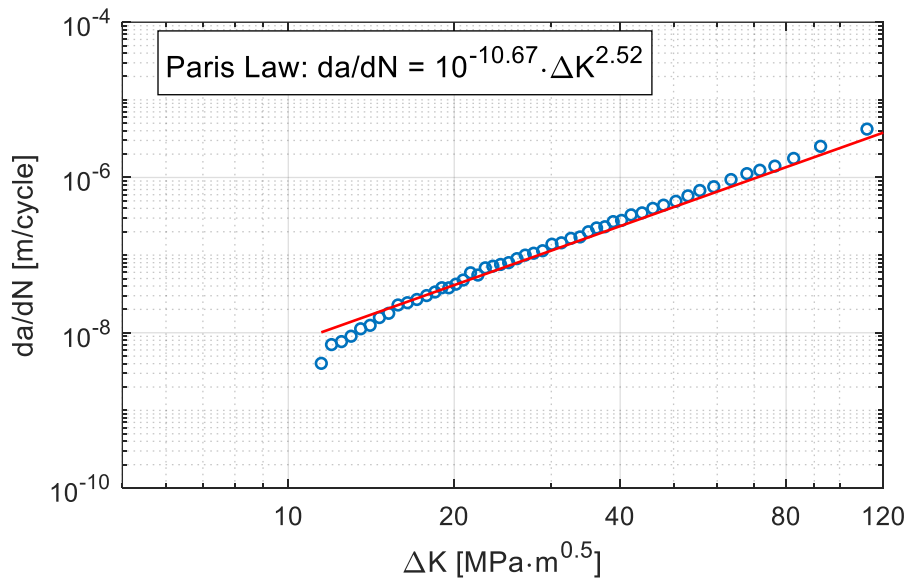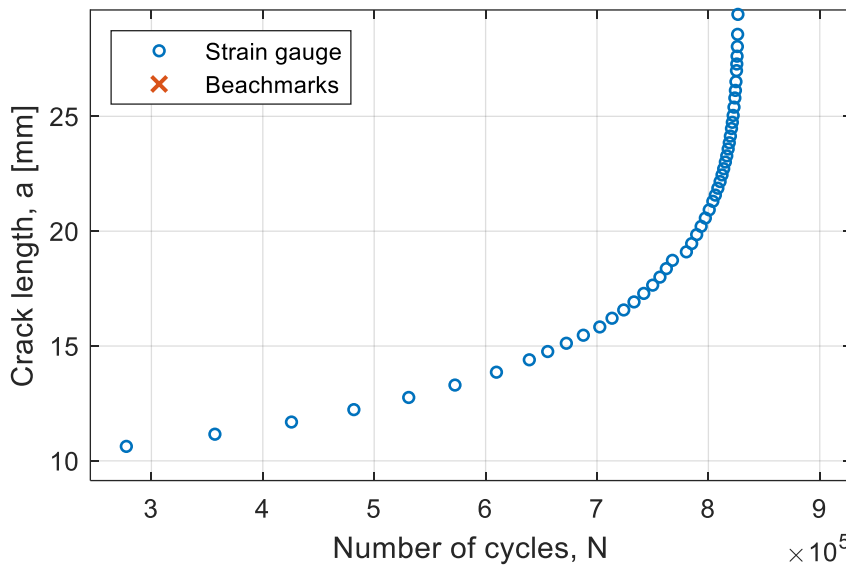

Figure 40: Crack growth rate versus stress intensity factor range for the L1AB-2 specimen.

L1AB-4

The first step of the pre-cracking phase was conducted for the same number of cycles as the L1AB-2 specimen, but between step 2 and step 3 there was no correspondence of crack size measurement, according to the back-face strain gauge technique. Consequently, steps 2 and 3 were repeated and then the pre-cracking proceeded to the last step with no issues.

Table 21

Pre-cracking parameters of L1AB-4 specimen.

	L1AB-4		
Step	Lmax [N]	Frequency [Hz]	N
1	6000	40	28000
2	5000	40	10000+5000
3	4000	40	8000+5000
4	3200	40	30000
5	2600	40	30000

At the end of the pre-cracking phase, the crack size was 9.1 mm, corresponding to a stress intensity factor range of 10.2 Mpa√m as test initial value. The test was conducted with the parameters reported in Table 22:

Table 22

Test parameters for L1AB-4 specimen.

Lmax [N]	R	F [Hz]	N
2100	0.1	20	250000
1680	0.125	4	10000
2100	0.1	20	250000
1680	0.125	4	10000
2100	0.1	20	250000
1680	0.125	4	10000
2100	0.1	20	46675

During the measurement validation after the test, only two beachmarks were observed on the fracture surface.

The resulting crack size versus number of cycles plot is reported in Figure 41:

Figure 41: Crack size versus number of cycles plot for the L1AB-4 specimen

The data from the test were then processed with the secant method in order to obtain the crack growth rate versus stress intensity factor range plot (Figure 42):
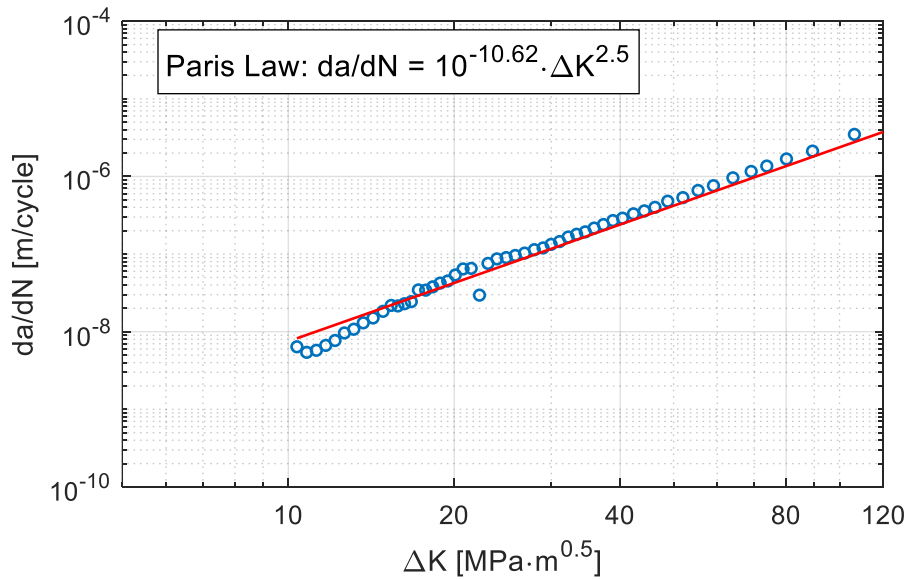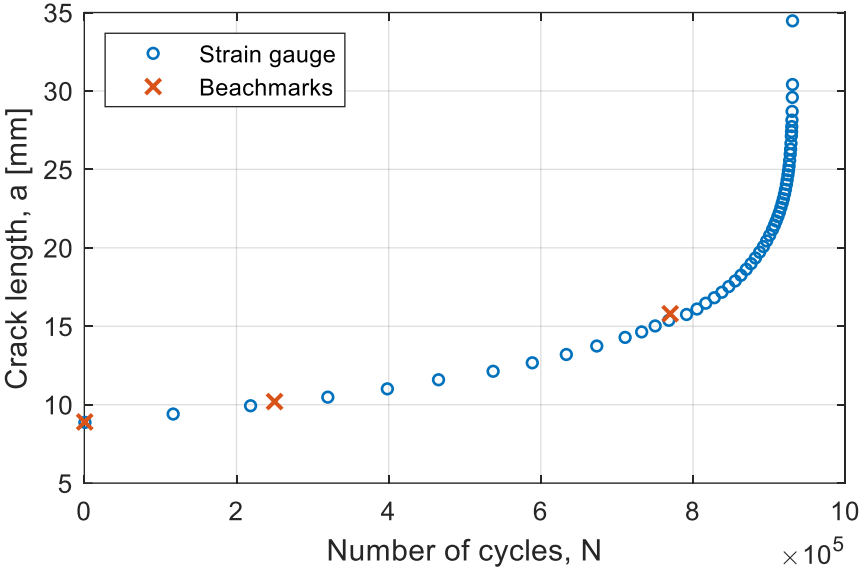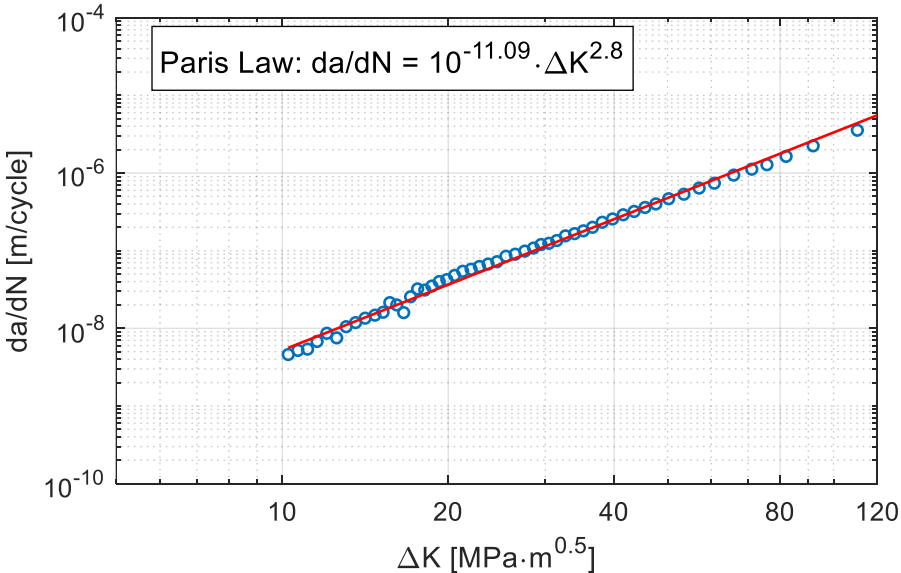

Figure 42: Crack growth rate versus stress intensity factor range for the L1AB-4 specimen.

L3MC-1

During the pre-cracking phase, there was a difference between the non-visual and visual measurement technique of about 1 mm, and in the validation after the test, this was attributed to the through-thickness crack curvature. It was decided to repeat the pre-cracking procedure from step 3, with a positive result in terms of measurements validation.

Table 23

Pre-cracking parameters of L3MC-1 specimen.

	L3MC-1			
Step	Lmax [N]	Frequency [Hz]	N_1	N_2
1	8800	40	27000	
2	7100	40	11000	
3	5700	40	14000	10000
4	4600	40	22000	25000
5	3700	40	50000	20000

At the end of the second pre-cracking phase, the crack size was 12.5 mm, corresponding to a stress intensity factor range of 10.5 Mpa√m as test initial value. The test was conducted with the parameters reported in Table 24:

Table 24

Test parameters for L3MC-1 specimen.

Lmax [N]	R	F [Hz]	N
3000	0.1	20	400000
2400	0.125	4	10000
3000	0.1	20	350000
2400	0.125	4	10000
3000	0.1	20	162152

The validation of the measurement was positive: 3 beachmarks were visible on the fracture surface, one from pre-cracking and two from the procedure during the test. The resulting crack size versus number of cycles plot is reported in Figure 43:
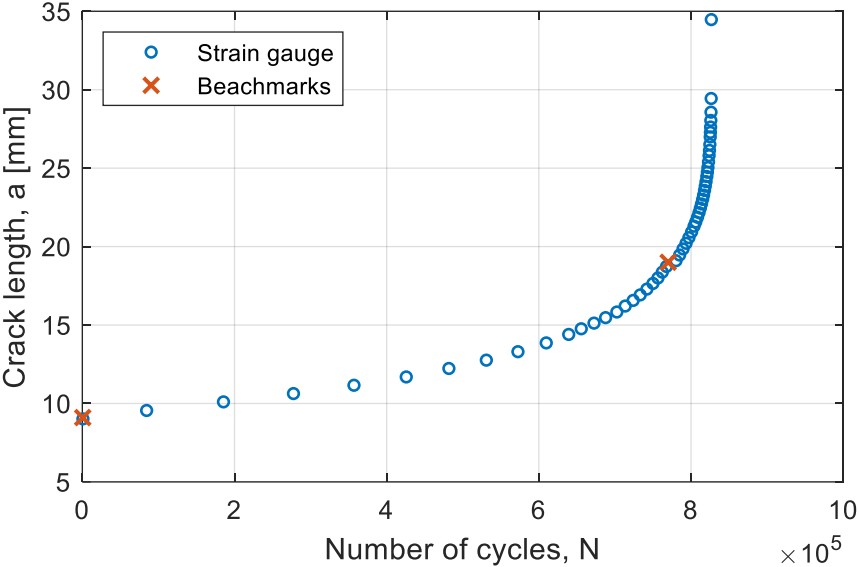
Figure 43: *Crack size versus number of cycles plot for the L3MC-1 specimen.*

The data from the test were then processed with the secant method in order to obtain the crack growth rate versus stress intensity factor range plot (Figure 44):
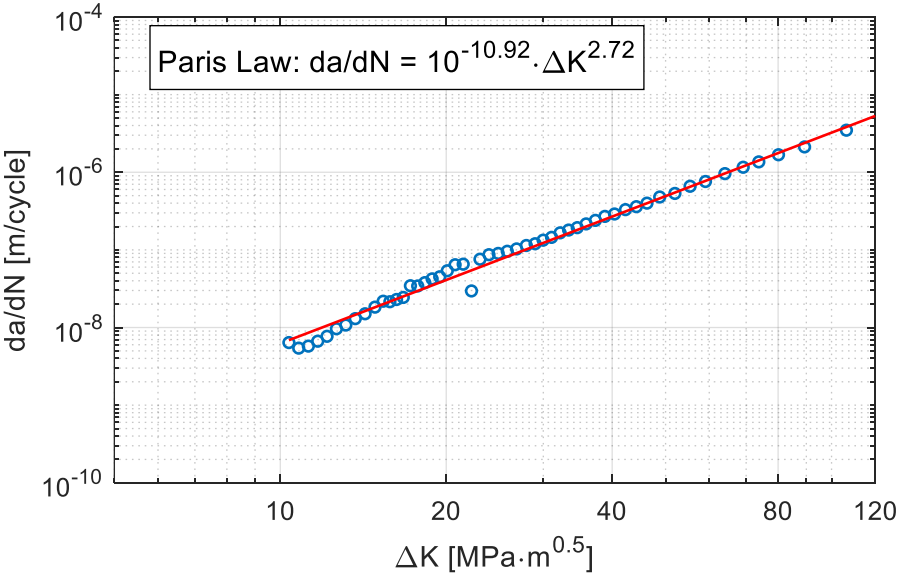

Figure 44: *Crack growth rate versus stress intensity factor range for the L3MC-1 specimen.*

L3MC-2

The pre-cracking phase was conducted smoothly for the first 3 steps, then a technical issue stopped the procedure for a short interruption (less than 10 minutes), with neglectable effects, according to the standard. However, it was decided to restart the pre-cracking with 5000 cycles of step 3. Both measurements on front and back validated the non-visual measurement technique.

Table 25

Pre-cracking parameters of L3MC-2 specimen.

Step	L3MC-2 Lmax [N]	Frequency [Hz]	N
1	8800	40	30000
2	7100	40	14000
3	5700	40	17000+5000
4	4600	40	19000
5	3700	40	34000

At the end of the second pre-cracking phase, the crack size was 11.9 mm, corresponding to a stress intensity factor range of 10.2 Mpa√m as test initial value. The test was conducted with the parameters reported in Table 26:

Table 26

Test parameters for L3MC-2 specimen.

Lmax [N]	R	F [Hz]	N
3000	0.1	20	400000
2400	0.125	4	10000
3000	0.1	20	350000
2400	0.125	4	10000
3000	0.1	20	295250

The validation of crack size measurement was positive, as 2 out of 3 beachmarks were clearly visible on the fracture surface.

The resulting crack size versus number of cycles plot is reported in Figure 45:
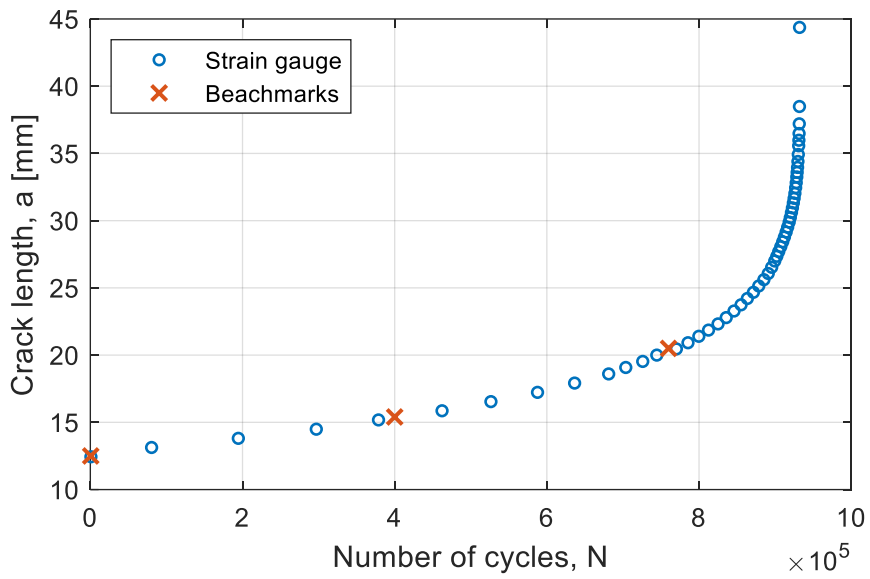

Figure 45: *Crack size versus number of cycles plot for the L3MC-2 specimen.*

The data from the test were then processed with the secant method in order to obtain the crack growth rate versus stress intensity factor range plot (Figure 46):
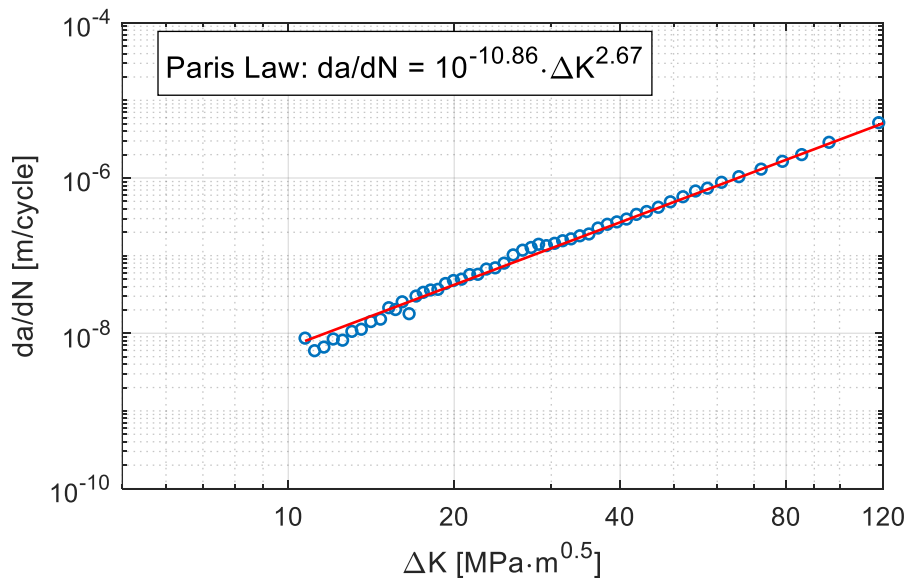

Figure 46: *Crack growth rate versus stress intensity factor range for the L3MC-2 specimen.*

L3AB-2

The pre-cracking phase was conducted with no issues, and the measurements was always in accordance step-by-step of the ΔK decreasing pre-cracking procedure.

Table 27

Pre-cracking parameters of L3AB-2 specimen.

	L3AB-2		
Step	Lmax [N]	Frequency [Hz]	N
1	8800	40	46000
2	7100	40	22000
3	5700	40	19000
4	4600	40	33000
5	3700	40	37500

Due to a technical issue, the first 400000 cycles of the test data are not available, but the interruption was a short one and the test was re-started immediately. For this reason, according to the available data, the test started with a crack size of 13.15 mm, corresponding to a stress intensity factor range of 11 Mpa√m as test initial value. The test was conducted with the parameters reported in Table 28:

Table 28

Test parameters for L3AB-2 specimen.

Lmax [N]	R	F [Hz]	N
3000	0.1	20	300000
2400	0.125	4	10000
3000	0.1	20	558164

For the same reason of above, the beachmarking procedure was conducted only one time. After the test, both beackmarks were visible on the fracture surface, the first from the test starting and the second from the beachmarking procedure. The resulting crack size versus number of cycles plot is reported in Figure 47:
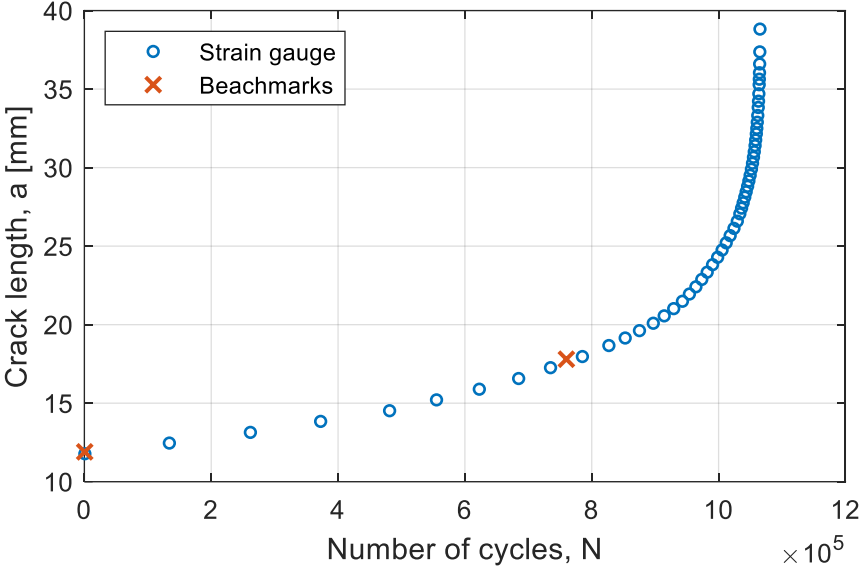
Figure 47: *Crack size versus number of cycles plot for the L3AB-2 specimen.*

The data from the test were then processed with the secant method in order to obtain the crack growth rate versus stress intensity factor range plot (Figure 48):
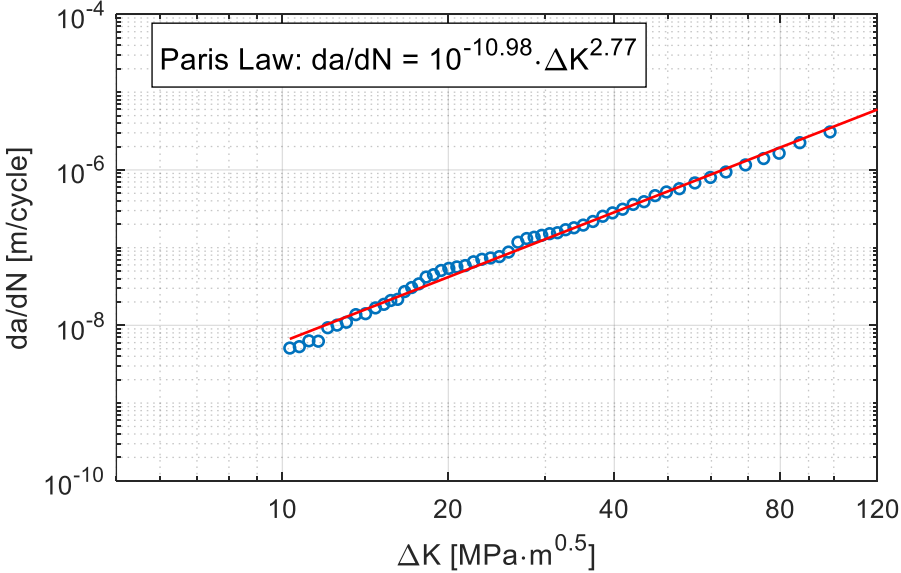

Figure 48: *Crack growth rate versus stress intensity factor range for the L3AB-2 specimen.*

L3AB-3

During the pre-cracking phase, no particular issues have been recorded. At the end of the last step, a short interruption occurred, and it was decided to make 14000 cycles before starting the test.

Table 29

Pre-cracking parameters of L3AB-3 specimen.

	L3AB-3		
Step	L_{max} [N]	Frequency [Hz]	N
1	8800	40	45500
2	7100	40	17000
3	5700	40	19000
4	4600	40	29000
5	3700	40	22700+14000

At the end of the pre-cracking phase, the crack size was 11.9 mm, corresponding to a stress intensity factor range of 10.2 Mpa√m as test initial value. The test was conducted with the parameters reported in Table 30:

Table 30

Test parameters for L3AB-3 specimen.

L_{max} [N]	R	F [Hz]	N
3000	0.1	20	400000
2400	0.125	4	10000
3000	0.1	20	350000
2400	0.125	4	10000
3000	0.1	20	445000

After the test, the crack size measurement was validated with the beachmarks comparison: 2 out of 3 beachmarks were visible on the fracture surface, and the validation was positive.

The resulting crack size versus number of cycles plot is reported in Figure 49:
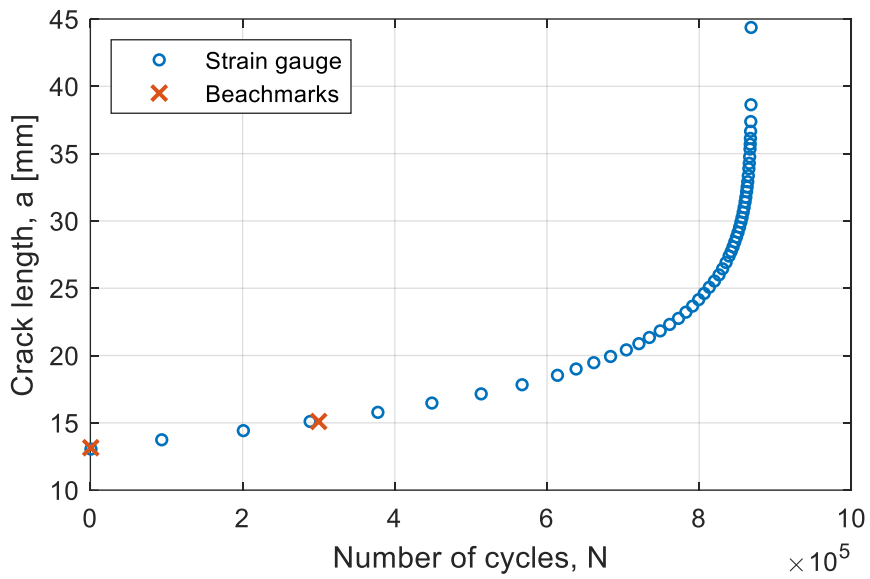

Figure 49: Crack size versus number of cycles plot for the L3AB-3 specimen.

The data from the test were then processed with the secant method in order to obtain the crack growth rate versus stress intensity factor range plot (Figure 50):
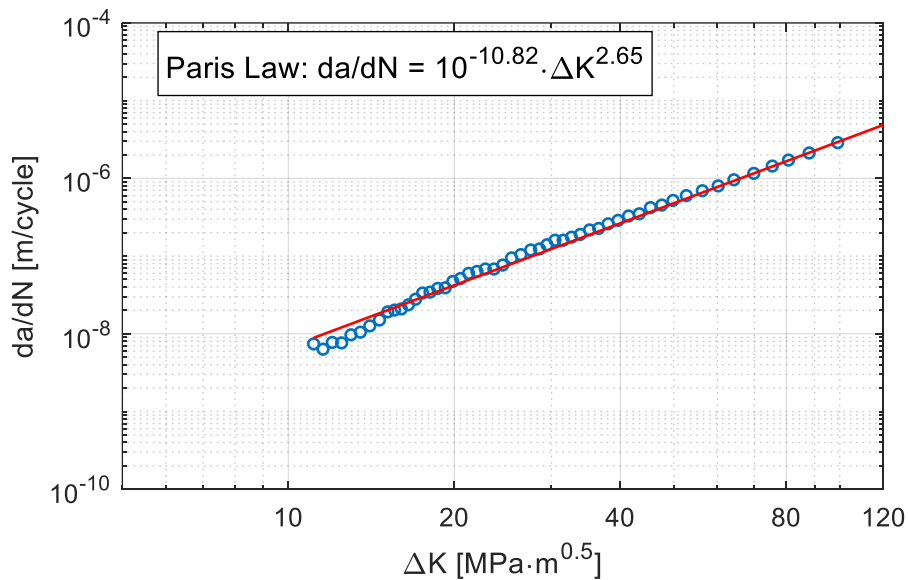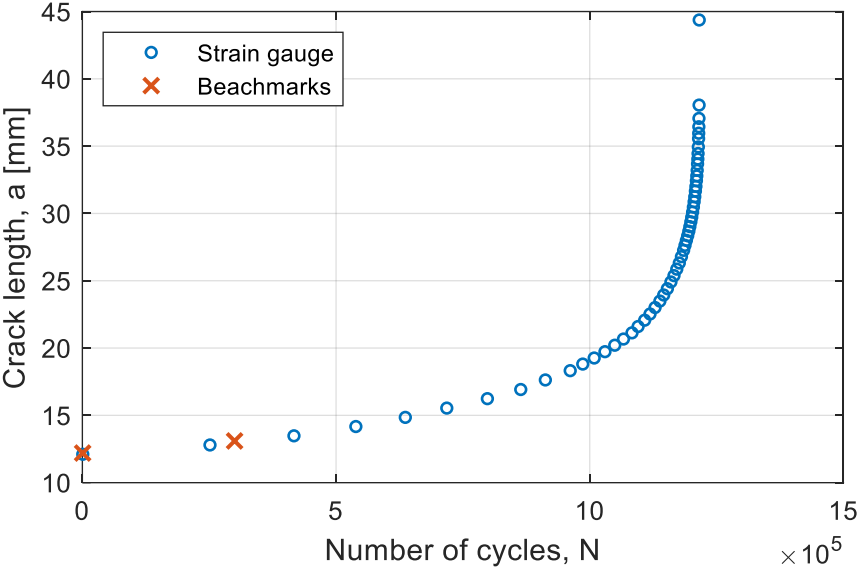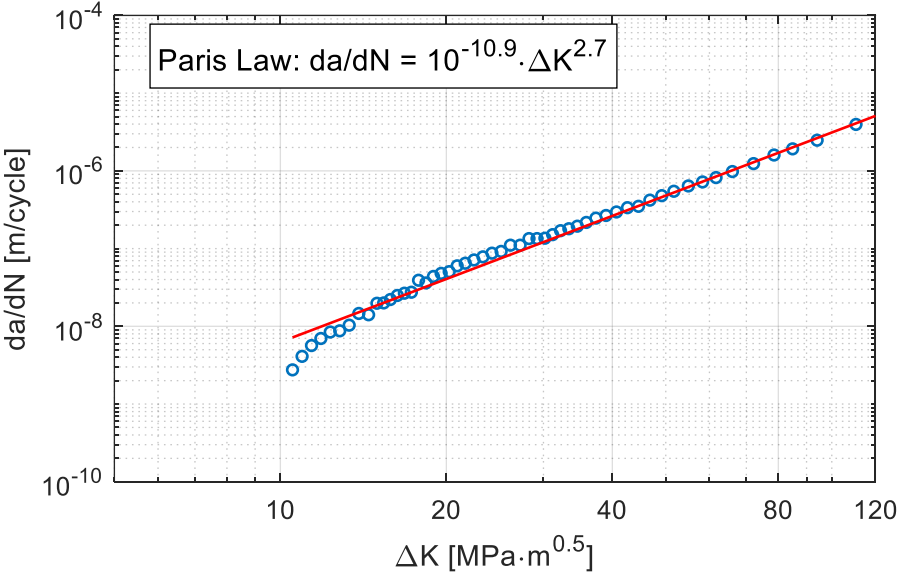

Figure 50: Crack growth rate versus stress intensity factor range for the L3AB-2 specimen.

3.2 Results summary

All the nine tests of this study have been made in accordance with the standard, and the validations in terms of crack requirements and crack size measurements were always respected. The obtained results are reported in Table 31 and Figure 51:

Table 31

Fatigue crack growth tests results in terms of Paris Law coefficients for all the tested specimens.

Test ID	Thickness [mm]	Condition	$C\left[\dfrac{m}{cycle}\dfrac{1}{(MPa\sqrt{m})^{n}}\right]$	n
L1-AB-1			$10^{-10.62}$	2.5
L1-AB-2		As-built	$10^{-11.09}$	2.8
L1-AB-4	5		$10^{-10.92}$	2.72
L1-MC-2		Machined	$10^{-10.73}$	2.58
L1-MC-4			$10^{-10.67}$	2.52
L3-AB-2		As-built	$10^{-10.82}$	2.65
L3-AB-3	6.4		$10^{-10.9}$	2.7
L3-MC-1		Machined	$10^{-10.86}$	2.67
L3-MC-2			$10^{-10.98}$	2.77

Figure 51: Fatigue crack growth rates versus stress intensity factor range for all the tests.

4 Discussions

Many problems associated with AM components can be associated with nature, size, distribution and morphology of internal defects. Moreover, the typical microstructure induced by the pr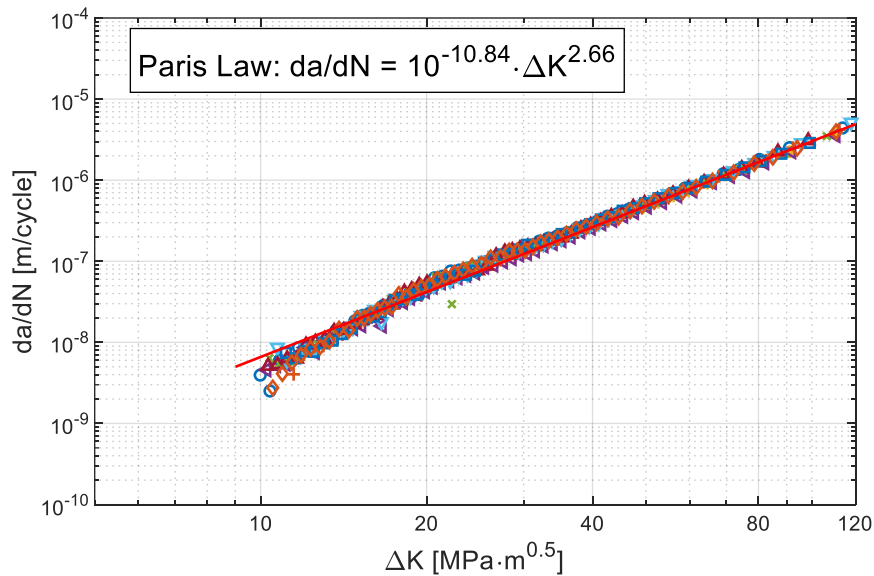ocess influences the mechanical behavior of the material, which can be significantly different from that of the same material obtained with traditional techniques. However, while the microstructure can be modified with post-process heat-treatment, such as the CA-H1025 for this study case, regarding the internal defects, the only way to limit their presence is to optimize the process parameters during the L-PBF production. The most significant process parameters are related to laser (laser power, spot size, focal offset distance), scan (scan velocity, hatch spacing, scan strategy), powder (particle size, shape and material, powder bed density, powder bed temperature, layer thickness) and build chamber (temperature, atmosphere). The high number of factors influencing the process result makes it complex to identify the causes of defects, thus it's possible to focus on two parameters: laser power and scanning velocity.
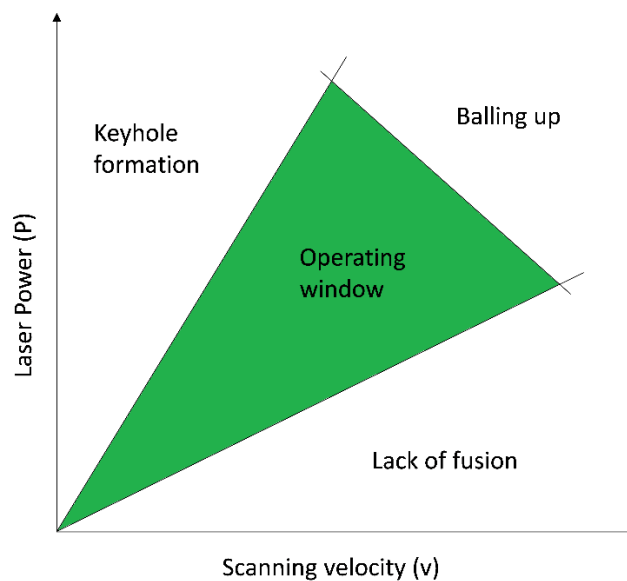

Figure 52: Qualitative representation of defects present in AM components as a function of laser power and scan velocity.

In order to correlate the macro-scale mechanical performance found with the laboratory tests, with a particular focus on the effects of thickness and surface condition, to the microstructural properties, a metallographic characterization was

made, through optical microscope as well as Scanning Electronic Microscope (SEM). The purpose was to understand whether the microstructure could justify the neglectable influence of thickness and surface condition on the mechanical behavior. For the optical microscope analysis, two L3 specimens were considered (the L3MC-2 and L3AB-2), while for the SEM analysis, four specimens were considered (L1MC-2, L1AB-2, L3MC-2 and L3AB-2).

4.1 Optical Microscope analysis

The optical microscope analysis was made for 3 different sections of L3 specimens. In particular, the L3MC-2 front face, and the through-thickness L3MC-2 and L3AB-2 sections were observed. The samples were obtained from the specimens by cutting off with a silicon carbide blade, and then incorporated with phenolic resin at 170 °C and 250 bar for 5 minutes. Then, the samples have been mirror polished by several passes of sanding paper, with each pass having finer grain with respect to the previous one, before being observed.
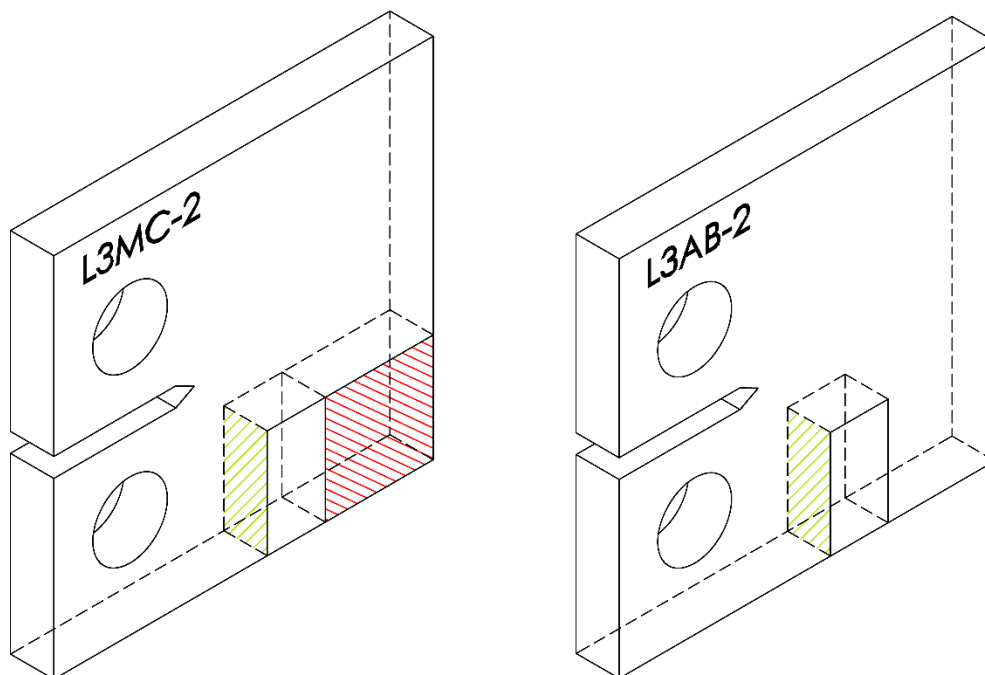
Figure 53: *Representation of the samples observed at the optical microscope: flat section (in red) and through-thickness sections (in green).*

Regarding the L3MC-2 front face, the observation showed a very low presence of defects, mainly having circular shape (Figure 54):
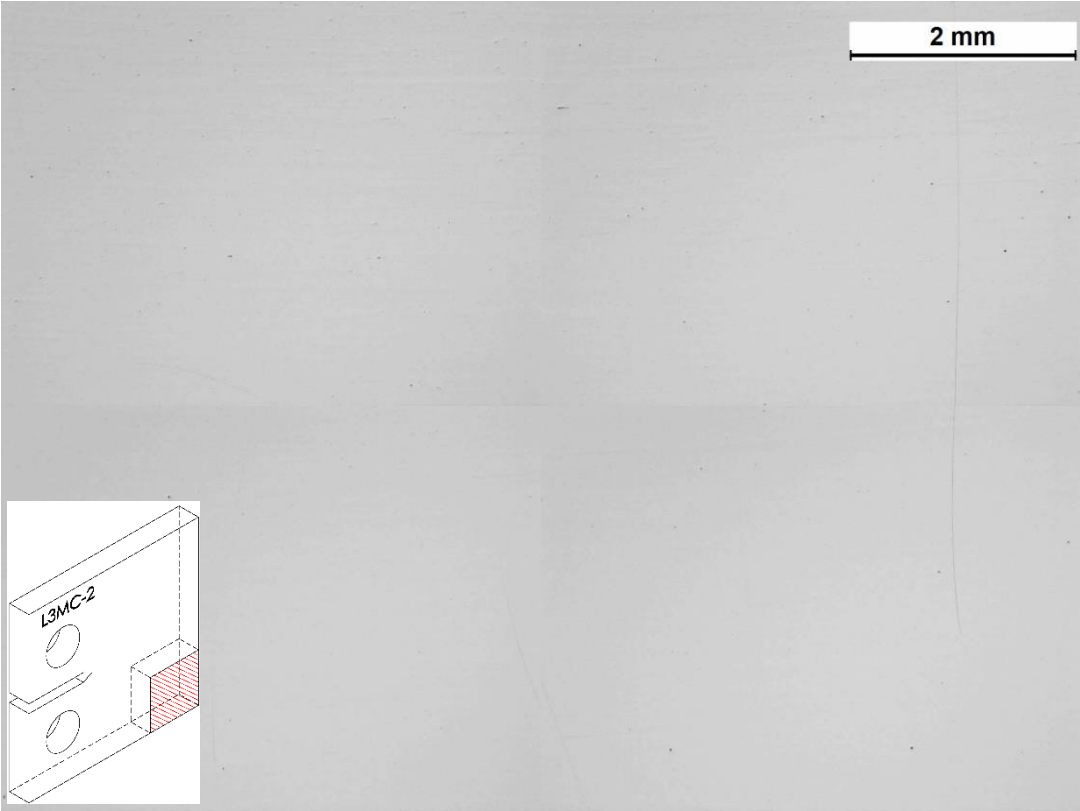
Figure 54: *overview of the incidence of defects in front sample of L3MC-2 specimen.*

At higher magnifications, the analysis revealed the presence of defects identified as keyhole formations and lack of fusions. However, the size and density of the observed defects were extremely low and thus not significant for the characterization of macroscopic properties analyzed by the performed experimental tests.
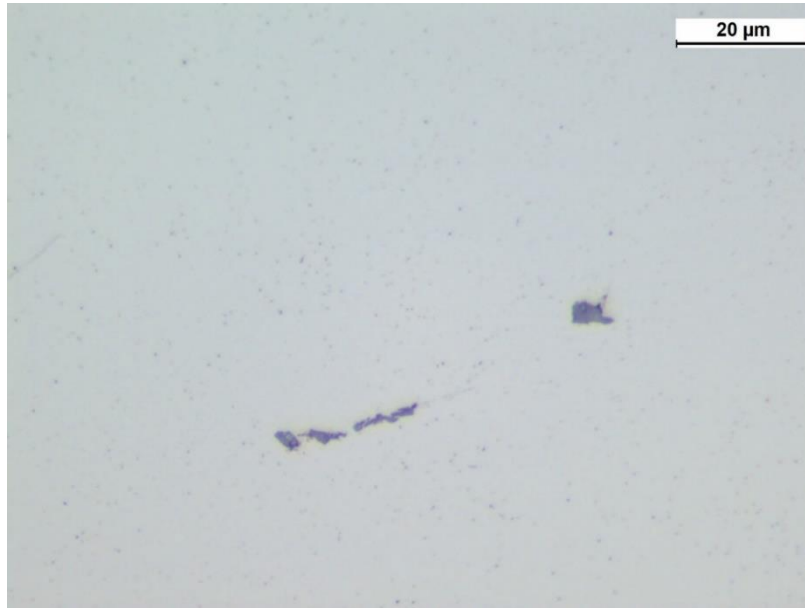
Figure 55: Defect detail of L3MC-2 specimen.

After a defect investigation of the sample, microstructure analysis was conducted by means of chemical etching. Specifically, the Vilella's reagent was used to reveal the presence of martensite and any existing ferrite and carbides. The reagent is composed of 1 g of picric acid, 5 ml of hydrochloric acid and 100 ml of ethanol, and the sample was immersed in it for one minute at room temperature before being observed under the microscope.

Figure 56: Microstructure of the L3MC-2 front sample at the optical microscope after chemical etching.

An initial observation revealed a high degree of homogeneity in the microstructure (Figure 56). This can be attributed to the heat treatment carried out on the samples, which completely eliminated the typical layer effect observed in components obtained through AM.

At higher magnifications, acicular-shaped martensite grains can be observed, whose non-directionality confirms the isotropy of the material (Figure 57).

Figure 57: Detail of the L3MC-2 front sample microstructure.

The second sample taken from the L3MC-2 specimen was observed to analyze its through-thickness section. The result showed a sporadic presence of defects of very limited size (Figure 58). As discussed for the frontal section, it can be concluded that these defects have a neglectable effect on the macroscopic properties of the material.
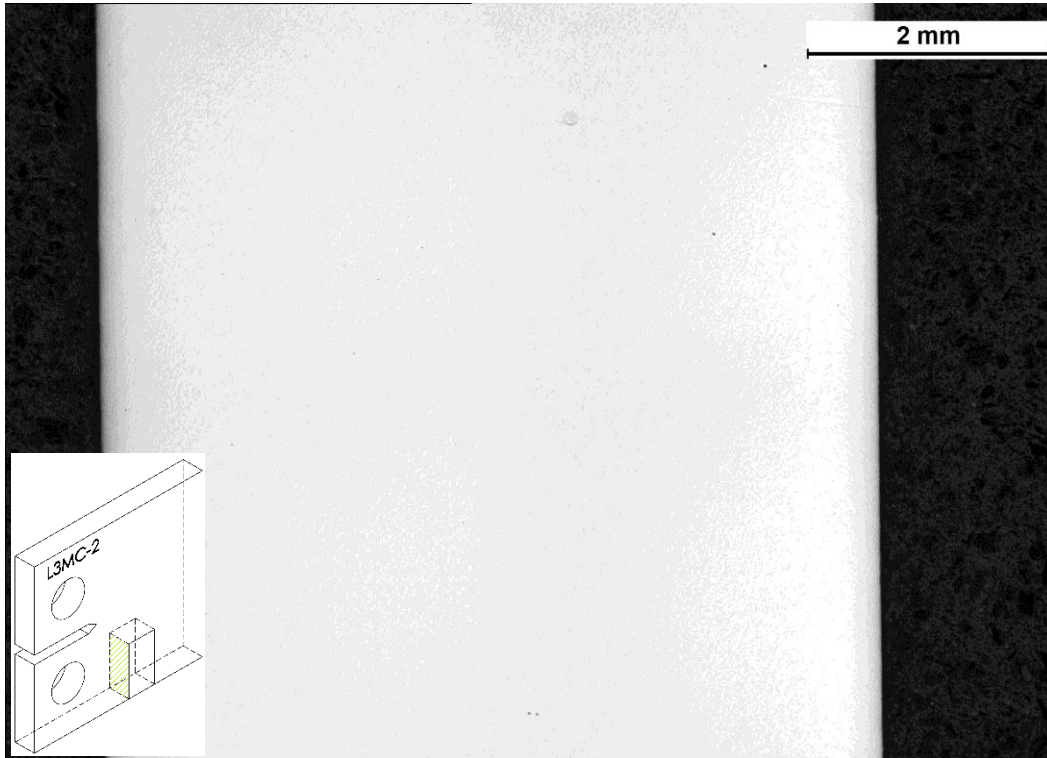
Figure 58: Overview of the incidence of defects in through-thickness sample of L3MC-2 specimen.

Similar to what was done for the front section, higher magnifications were used to appreciate the nature, size and morphology of the defects present (Figure 59).
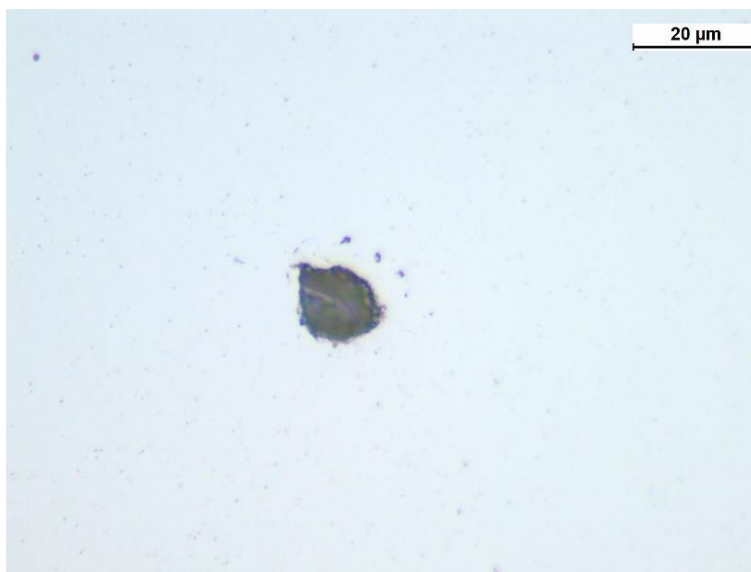
Figure 59: Defect detail of the L3MC-2 through-thickness specimen.

In this case, a visual analysis was performed to quantify the size and amount of defects present in the considered section. The results were then reported in a graph that shows the number of defects versus the equivalent circular diameter (Figure 60). In this instance, a 37 mm^2 area was subjected to analysis, and the results yielded an insignificantly low incidence of defects, with a maximum dimension of 25 µm, a mean value of 11 µm, and a standard deviation of 6 µm.
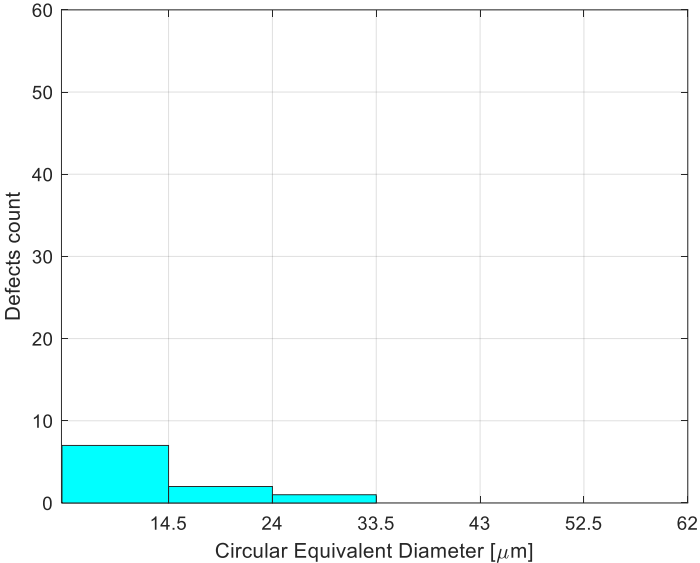
Figure 60: *Number of defects versus circular equivalent diameter of the L3MC-2 through-thickness sample.*

Subsequently, the microstructure of the sample subjected to chemical etching was observed (Figure 61). Vilella's reagent was utilized in this instance as well, with the sample being subjected to immersion in the solution for a duration of one minute at room temperature.
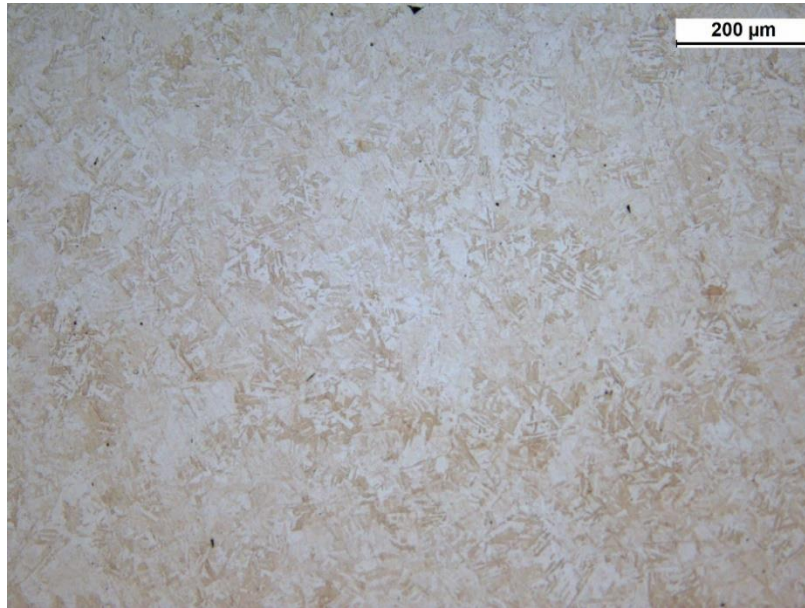
Figure 61: Microstructure of the L3MC-2 through-thickness sample at the optical microscope after chemical etching.

Upon comparison with the findings obtained from the front sample, a significant resemblance was observed in the microstructure of the sections analyzed, thereby confirming the isotropic characteristics of the material. At higher magnifications, martensite grains can be distinguished, which are characterized by non-directionality (Figure 62).
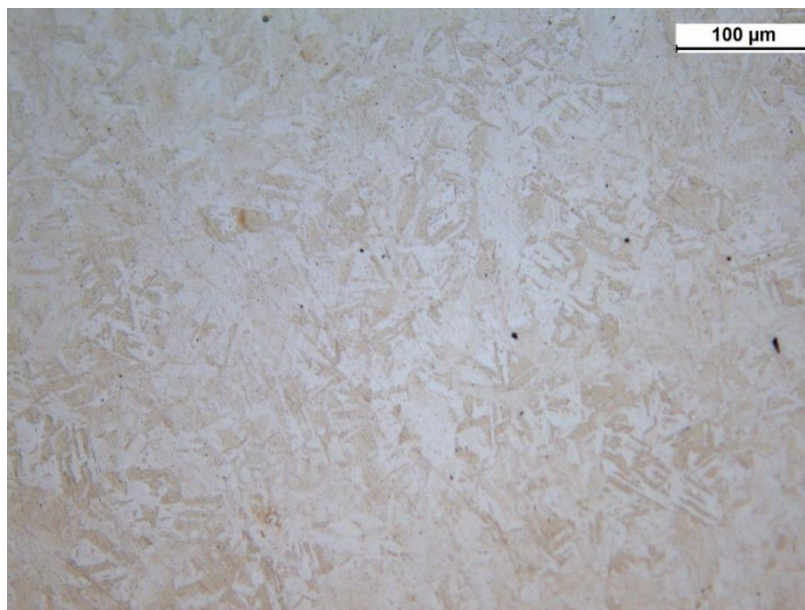
Figure 62: Detail of the L3MC-2 through-thickness sample microstructure.

The final sample examined through the optical microscope was obtained from the L3AB-2 specimen. To enable a convenient comparison of the findings with the same section of the L3MC-2 specimen, an identical methodology was adopted.

The examination entailed an assessment of the general condition of the section in terms of incidence of defects (Figure 63). Similar to the previous observations, the defects have an irregular distribution, small size, and predominantly spherical features.

Figure 63: Overview of the incidence of defects in through-thickness sample of L3AB-2 specimen.

Similar to what was done for the front section, higher magnifications were used to appreciate the nature, size and morphology of the defects present (Figure 64).
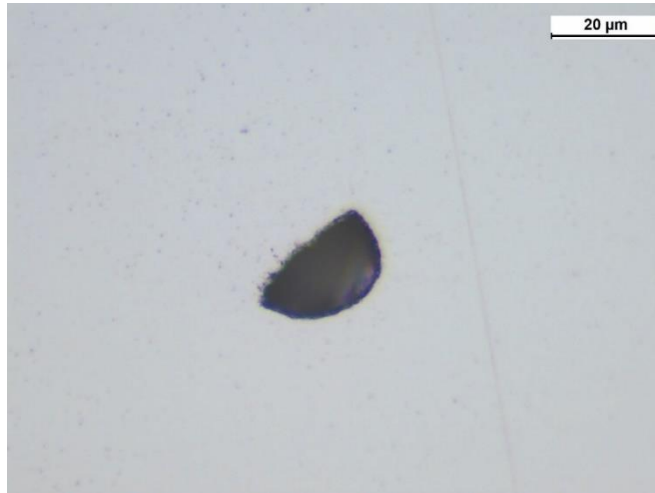
Figure 64: *Defect detail of the L3AB-2 through-thickness specimen.*

Despite the relatively higher incidence rate in absolute terms, it can be inferred that the observed defects do not significantly impact the macroscopic mechanical properties studied and identified through the conducted tests. The results were then reported in a graph that shows the number of defects versus the equivalent circular diameter (Figure 65). In this instance, a 36 mm^2 area was subjected to analysis, and the results yielded an insignificantly low incidence of defects, with a maximum dimension of 45 µm, a mean value of 16 µm, and a standard deviation of 9 µm.
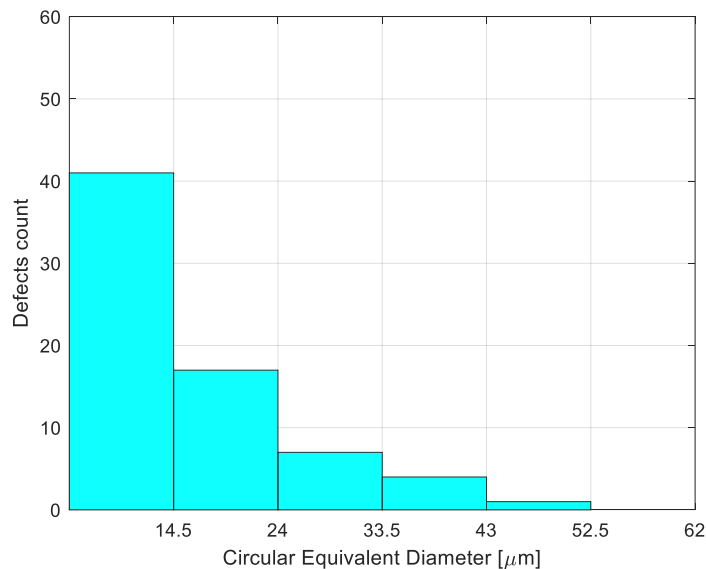
Figure 65: *Number of defects versus circular equivalent diameter of the L3AB-2 through-thickness sample.*

The use of metallographic etching in microstructural analysis facilitates a comparative evaluation between distinct specimens. The present sample was treated with identical reagents and parameters employed in prior observations (Figure 66).

Figure 66: Microstructure of the L3AB-2 through-thickness sample at the optical microscope after chemical etching.

Figure 67: Detail of the L3AB-2 through-thickness sample microstructure.

The last optical microscope analysis was conducted to comparatively assess the surface conditions of specimens AB (Figure 68) and MC (Figure 69). Specifically, the outer surface of the analyzed samples was examined under high magnification.

Figure 68: *Surface condition detail of L3AB-2 through-thickness sample.*
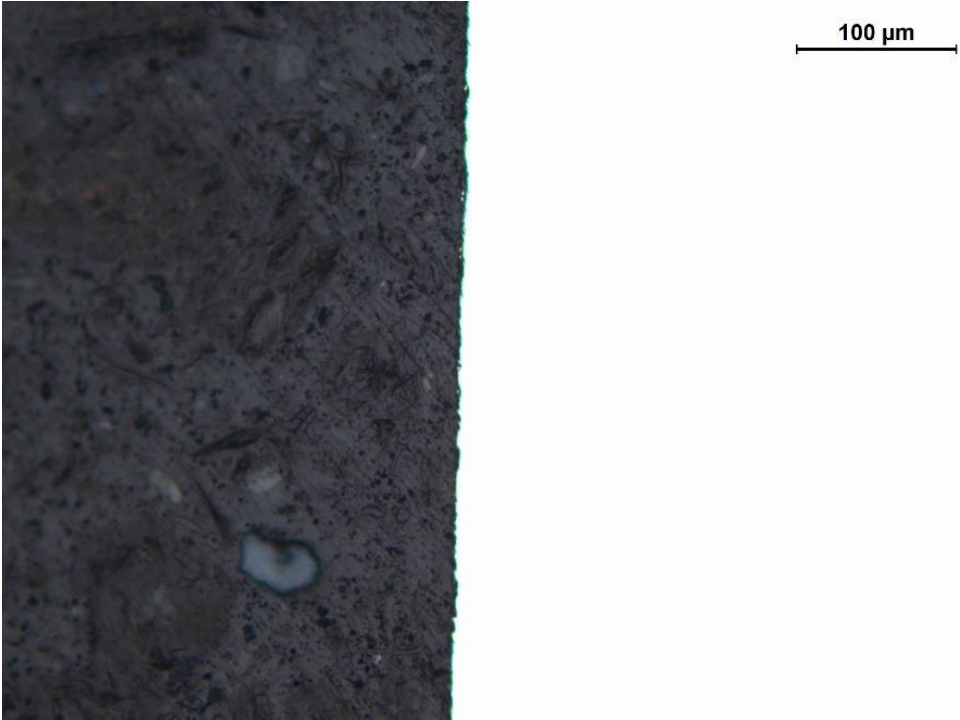
Figure 69: *Surface condition detail of L3MC-2 through-thickness sample.*

As commonly acknowledged, the fatigue life of mechanical components is significantly affected by their surface condition. The surface serves as the origin of crack nucleation, and typically, specimens with higher surface roughness exh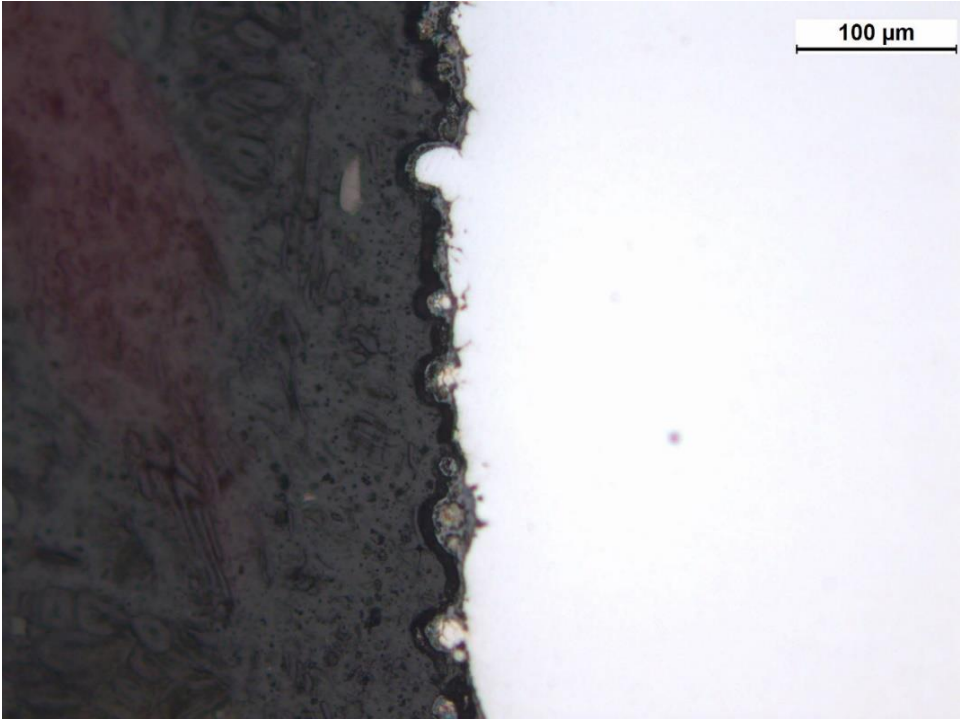ibit a reduced fatigue life. While the surface disparity between specimens AB and MC is discernible, it is worth noting that in this case, the type of specimen, due to its geometry and loading conditions, covers possible effects related to most favorable conditions for the crack to initiate due to the surface roughness. The crack, as expected, initiates from the notch surface, which was uniformly produced through the employment of EDM for all specimens. The investigation of different surface conditions was conducted with the aim to assess if the surface roughness could affect somehow the propagation of the crack in the component. However, the findings in section 3.2 confirm that no effects can be detected in the propagation of the crack not even in its early stage during the pre-cracking phase, with both AB and MC specimens that showed similar features.

4.2 Scanning Electronic Microscope Analysis

The fracture surfaces of four specimens were examined through a Scanning Electron Microscope (SEM). Three distinct regions of interest were studied in each specimen: crack initiation zone, fatigue crack zone and ductile fracture zone. The comparison of analogous zones on the fracture surfaces facilitated to understand the fracture mechanisms and the detection of any possible distinctions.
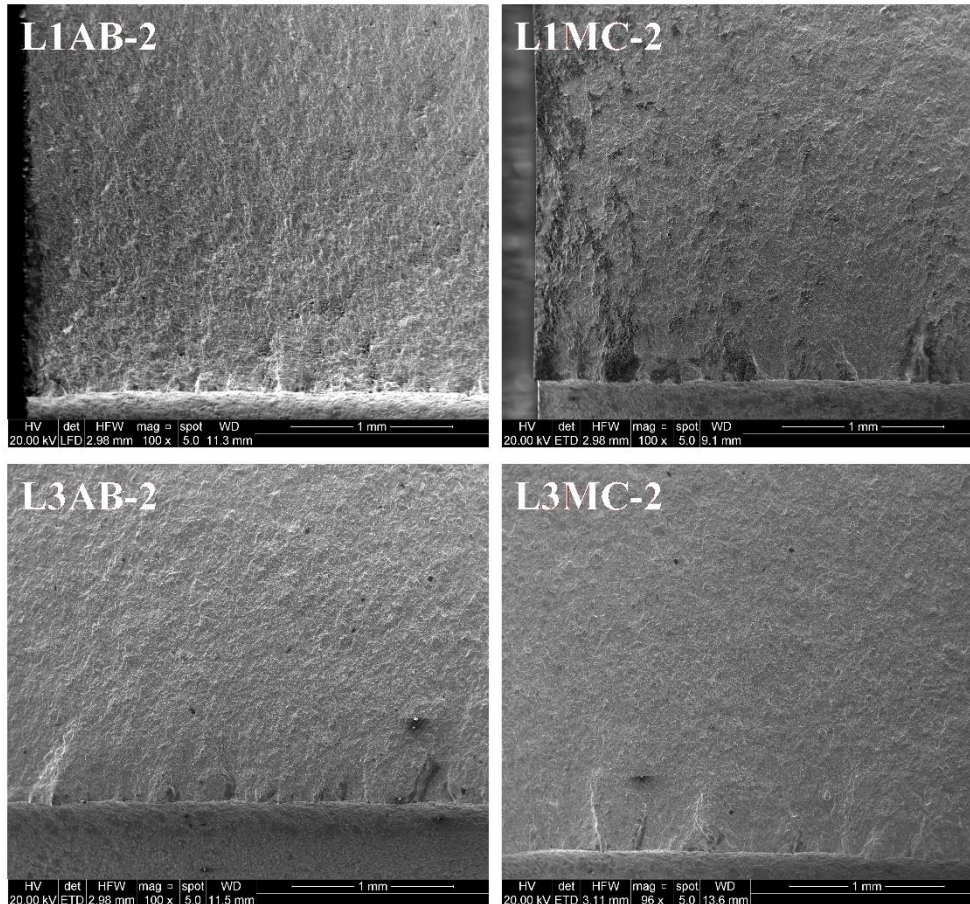
Figure 70: L1MC-2, L1AB-2, L3MC-2 and L3AB-2 fracture surfaces comparison in the crack initiation zone.

The presence of numerous nucleation sites along the thickness of the specimens during the crack initiation zone is noteworthy. The density of these sites near the notch dictates the morphology of the crack-front during the early stages of pre-cracking. the crack-front curvature during this phase can be ascribed to the distribution of defects, although the low amount of these defects leads to the settlement of the crack-front, rendering it almost linear by the end of the pre-cracking phase.
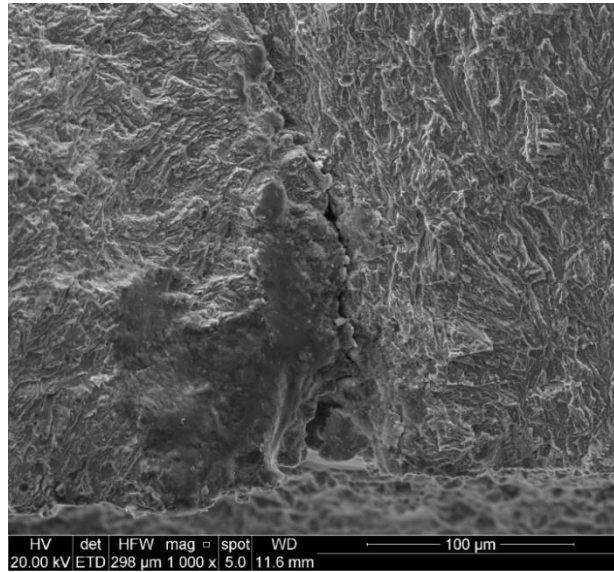
Figure 71: *Detail of L3AB-2 fracture surface in the crack initiation zone.*

The second region examined at the SEM was the fatigue crack zone:
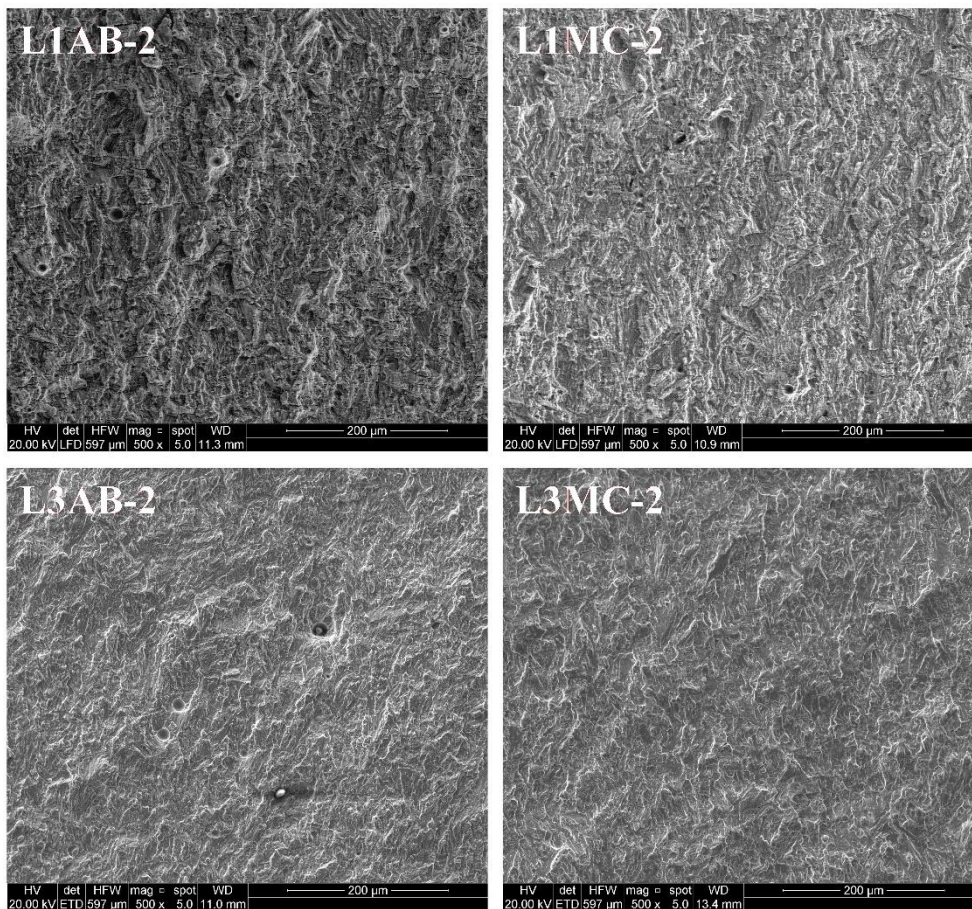
Figure 72: *L1MC-2, L1AB-2, L3MC-2 and L3AB-2 fracture surfaces comparison in the fatigue crack zone.*

Concerning this region, the similarity of the fracture surfaces among the different specimens is discernible. The sparse occurrence of defects identified through optical microscope examination is corroborated by SEM observations.
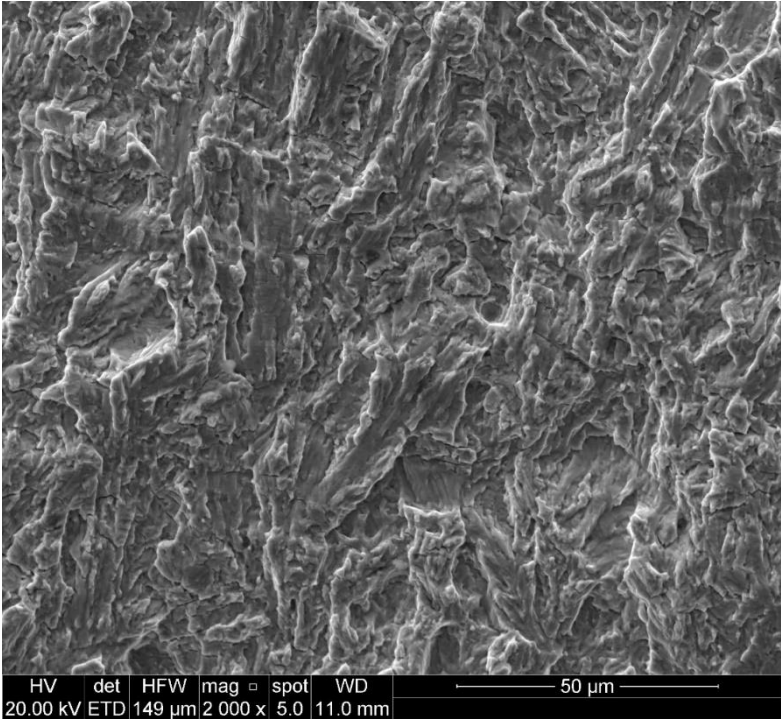
Figure 73: Detail of L3AB-2 fracture surface in the fatigue crack zone.

The last region of the fracture surfaces analyzed was the ductile fracture zone, which corresponds to the conclusive stages of the experiment. Analogous to the macroscopic behavior exhibited by the tests, the likeness between the various specimens analyzed is evident in this scenario as well.
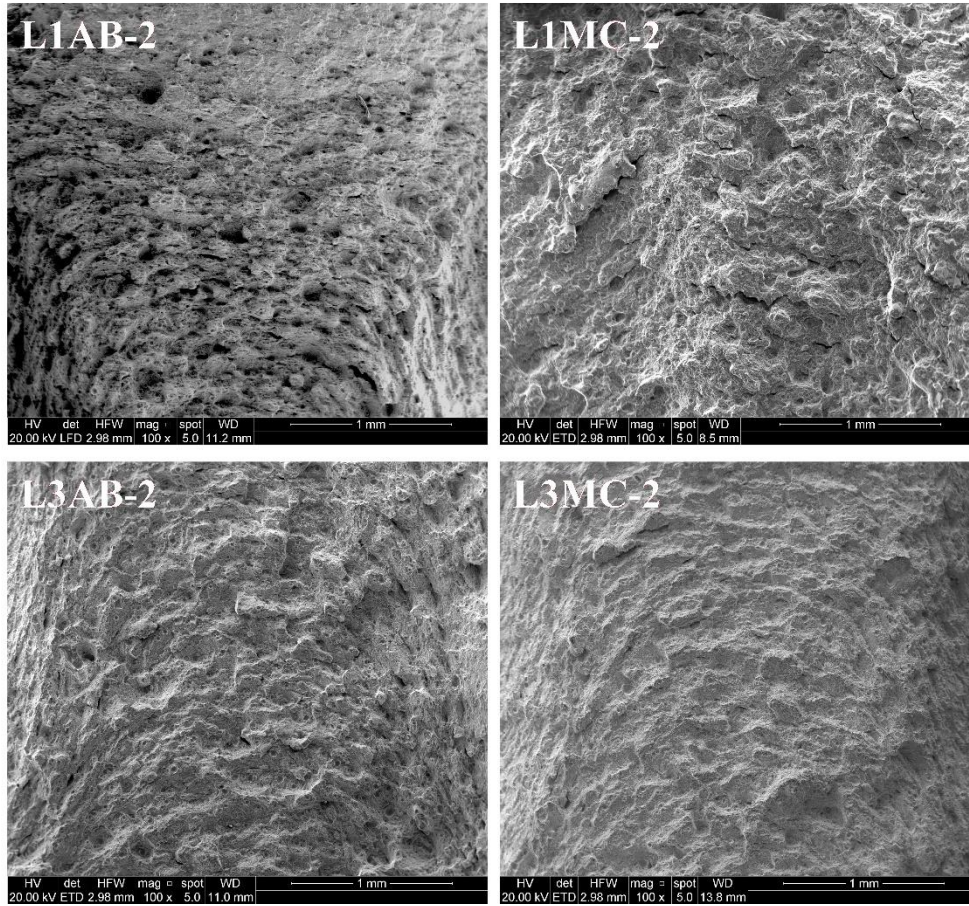
Figure 74: L1MC-2, L1AB-2, L3MC-2 and L3AB-2 fracture surfaces comparison in the ductile fracture zone.
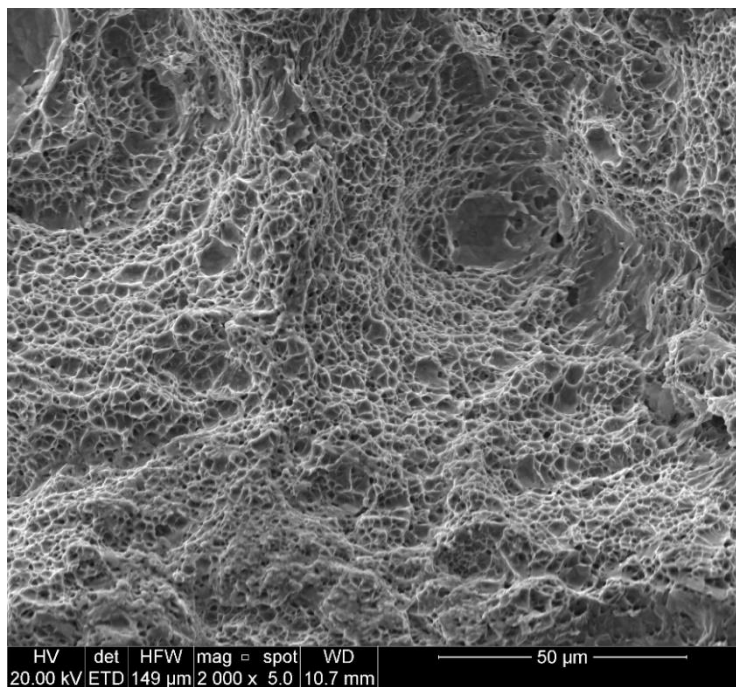
Figure 75: Detail of L3AB-2 fracture surface in the ductile fracture zone.

5 Conclusions and Recommendations

5.1 Conclusions

Additive Manufacturing is a central technology in Industry 4.0, but even if the potential of this technology is obvious, the application depends on a better understanding of the mechanical characteristics deriving from this process. In recent decades, the typical properties of Classical Mechanics, such as static and fatigue behavior have been thoroughly investigated for a large amount of different materials. In the last few years, the focus moved to the Linear Elastic Fracture Mechanics, with the aim to correlate the Fatigue Crack Growth behavior with the process parameters and the subsequent microstructure. Two fundamental factors characterizing components in Additive Manufacturing are the poor surface quality and the geometric freedom. In this regard, this study aims to understand whether it is worthwhile to further machine surfaces and if there are any constraints to be imposed in terms of thickness in a possible topological and dimensional analysis. This study reported an experimental campaign carried out on 17-4 PH Stainless Steel fabricated via Laser Powder Bed Fusion. The Fatigue Crack Growth behavior was analyzed through dedicated Compact Tensile specimen tests, with the objective of quantifying the mechanical properties of this martensitic steel and assessing the influence of thickness and surface condition on the material behavior. The results of this work revealed that:

- No appreciable effect on the Fatigue Crack Growth behavior can be detected with changing the specimen thickness in the range considered.
- Although the effect of the surface conditions on the fatigue initiation phase are well known, this has no effect on the stable crack propagation stage of the fatigue failure.
- The CA-H1025 heat treatment has been proved to confer isotropy to the material and to completely homogenize the material as proved by the microstructure analysis carried out using both optical microscope and Scanning Electron Microscope.

To sum up, on the base of the results of this work, heat treatments are recommended due to their beneficial effects; indeed, if properly defined in terms of their parameters (temperature and time), they result in an homogeneous microstructure, and the typical

anisotropic features induced by the Additive Manufacturing process should not be considered an issue. Dealing with the surface condition, it has been observed that it has no influence on Fatigue Crack Growth behavior; however, as it is well known, it reduces the material fatigue performance, acting mainly in the initial phase of the fatigue failure, providing favorable locations for the fatigue crack to initiate, an effect that must not be neglected when dealing with the fatigue design of AM components.

5.2 Recommendations for future research

The findings of this investigation advance the understanding of the mechanical properties of 17-4 Precipitation Hardening Stainless Steel produced via Laser Powder Bed Fusion, thereby laying a foundation for the design and production of components. However, the multitude of parameters influencing material properties makes it challenging to determine the effect of each parameter and optimize them. Within the scope of this study, no influence of thickness was found in the considered range. However, the examined range is small, and therefore, effects on different thicknesses cannot be excluded a priori. Additionally, a study considering a wider range of load ratios in the tests is also recommended. Finally, investigating the threshold region would serve to complete the characterization of the material's Fatigue Crack Growth curve, as it is well-recognized that the major sources of error in determining the number of cycles for the crack to reach its critical length resulting in the final failure of the component derive from the parameters established within this region. All this data collection, in addition to the literature background, can give a basement for the development of numerical models able to predict the behavior of additively manufactured components.

Bibliography

[1] J.-H. Wu and C.-K. Lin, "Tensile and Fatigue Properties of 17-4 PH Stainless Steel at High Temperatures."

[2] U. K. Viswanathan, S. Banerjee, and R. Krishnan, "Effects of Aging on the Microstructure of 17-4 PH Stainless Steel," 1988.

[3] M. Shellabear and O. Nyrhilä, "Whitepaper MATERIALS FOR DIRECT METAL LASER-SINTERING." [Online]. Available: www.eos.info.

[4] L. Facchini, N. Vicente, I. Lonardelli, E. Magalini, P. Robotti, and M. Alberto, "Metastable austenite in 17-4 precipitation-hardening stainless steel produced by selective laser melting," *Adv Eng Mater*, vol. 12, no. 3, pp. 184–188, Mar. 2010, doi: 10.1002/adem.200900259.

[5] L. E. Murr *et al.*, "Microstructures and Properties of 17-4 PH Stainless Steel Fabricated by Selective Laser Melting," *Journal of Materials Research and Technology*, vol. 1, no. 3, pp. 167–177, 2012, doi: https://doi.org/10.1016/S2238-7854(12)70029-7.

[6] H. K. Rafi, D. Pal, N. Patil, T. L. Starr, and B. E. Stucker, "Microstructure and Mechanical Behavior of 17-4 Precipitation Hardenable Steel Processed by Selective Laser Melting," *J Mater Eng Perform*, vol. 23, no. 12, pp. 4421–4428, Dec. 2014, doi: 10.1007/s11665-014-1226-y.

[7] T. H. Becker, P. Kumar, and U. Ramamurty, "Fracture and fatigue in additively manufactured metals," *Acta Materialia*, vol. 219. Acta Materialia Inc, Oct. 15, 2021. doi: 10.1016/j.actamat.2021.117240.

[8] P. D. Nezhadfar, K. Anderson-Wedge, S. R. Daniewicz, N. Phan, S. Shao, and N. Shamsaei, "Improved high cycle fatigue performance of additively manufactured 17-4 PH stainless steel via in-process refining micro-/defect-structure," *Addit Manuf*, vol. 36, Dec. 2020, doi: 10.1016/j.addma.2020.101604.

[9] T. M. Mower and M. J. Long, "Mechanical behavior of additive manufactured, powder-bed laser-fused materials," *Materials Science and Engineering A*, vol. 651, pp. 198–213, Jan. 2016, doi: 10.1016/j.msea.2015.10.068.

[10] P. D. Nezhadfar *et al.*, "Fatigue crack growth behavior of additively manufactured 17-4 PH stainless steel: Effects of build orientation and microstructure," *Int J Fatigue*, vol. 123, pp. 168–179, Jun. 2019, doi: 10.1016/j.ijfatigue.2019.02.015.

[11] E. Astm, "647: Standard test method for measurement of fatigue crack growth rates," *Annual book of ASTM standards*, vol. 3, pp. 591–630, 2011.

[12] H. J. Rack and D. Kalish, "The Strength, Fracture Toughness, and Low Cycle Fatigue Behavior of 17-4 PH Stainless Steel."

[13] A. Yadollahi, N. Shamsaei, S. M. Thompson, A. Elwany, and L. Bian, "Effects of building orientation and heat treatment on fatigue behavior of selective laser melted 17-4 PH stainless steel," *Int J Fatigue*, vol. 94, pp. 218–235, Jan. 2017, doi: 10.1016/j.ijfatigue.2016.03.014.

[14] A. Leybold-Herbert, "Axial-load fatigue tests on 17-7 ph stainless steel under constant-amplitude loading, NASA TN D-439 62 71013," *National Aeronautics and Space Administration, Langley Research Center Langley Field, Va.(October 1960)*, 1960.

[15] A. Yadollahi, M. Mahmoudi, A. Elwany, H. Doude, L. Bian, and J. C. Newman, "Effects of crack orientation and heat treatment on fatigue-crack-growth behavior of AM 17-4 PH stainless steel," *Eng Fract Mech*, vol. 226, Mar. 2020, doi: 10.1016/j.engfracmech.2020.106874.

[16] A. Yadollahi, M. Mahmoudi, A. Elwany, H. Doude, L. Bian, and J. C. Newman, "Effects of crack orientation and heat treatment on fatigue-crack-growth behavior of AM 17-4 PH stainless steel," *Eng Fract Mech*, vol. 226, Mar. 2020, doi: 10.1016/j.engfracmech.2020.106874.

[17] S. Romano, P. D. Nezhadfar, N. Shamsaei, M. Seifi, and S. Beretta, "High cycle fatigue behavior and life prediction for additively manufactured 17-4 PH stainless steel: Effect of sub-surface porosity and surface roughness," *Theoretical and Applied Fracture Mechanics*, vol. 106, Apr. 2020, doi: 10.1016/j.tafmec.2020.102477.

[18] S. Romano, P. D. Nezhadfar, N. Shamsaei, M. Seifi, and S. Beretta, "High cycle fatigue behavior and life prediction for additively manufactured 17-4 PH stainless steel: Effect of sub-surface porosity and surface roughness," *Theoretical and Applied Fracture Mechanics*, vol. 106, Apr. 2020, doi: 10.1016/j.tafmec.2020.102477.

[19] V. S. Raja and T. Shoji, *Stress corrosion cracking: theory and practice*. Elsevier, 2011.

[20] "Tokyo Measuring Instruments Lab."

[21] J. C. Newman, Y. Yamada, and M. A. James, "Back-face strain compliance relation for compact specimens for wide range in crack lengths," *Eng Fract Mech*, vol. 78, no. 15, pp. 2707–2711, Oct. 2011, doi: 10.1016/j.engfracmech.2011.07.001.

[22] A. Ermakova, S. Ganguly, J. Razavi, F. Berto, and A. Mehmanparast, "Corrosion-fatigue crack growth behaviour of wire arc additively manufactured ER70S-6 steel parts in marine environments," *European Journal of Mechanics, A/Solids*, vol. 96, Nov. 2022, doi: 10.1016/j.euromechsol.2022.104739.